

Scalable non-separable spatio-temporal Gaussian process models for large-scale short-term weather prediction

Tim Gyger^{*†}

Reinhard Furrer[†]

Fabio Sigrist^{‡*}

February 4, 2026

Abstract

Monitoring daily weather fields is critical for climate science, agriculture, and environmental planning, yet fully probabilistic spatio-temporal models become computationally prohibitive at continental scale. We present a case study on short-term forecasting of daily maximum temperature and precipitation across the conterminous United States using novel scalable spatio-temporal Gaussian process methodology. Building on three approximation families — inducing-point methods (FITC), Vecchia approximations, and a hybrid Vecchia-inducing-point full-scale approach (VIF) — we introduce three extensions that address key bottlenecks in large space-time settings: (i) a scalable correlation-based neighbor selection strategy for Vecchia approximations with point-referenced data, enabling accurate conditioning under complex dependence structures, (ii) a space-time kMeans++ inducing-point selection algorithm, and (iii) GPU-accelerated implementations of computationally expensive operations, including matrix operations and neighbor searches. Using both synthetic experiments and a large NOAA station dataset containing approximately 1.7 million space-time observations, we analyze the models with respect to predictive performance, parameter estimation, and computational efficiency. Our results demonstrate that scalable Gaussian process models can yield accurate continental-scale forecasts while remaining computationally feasible, offering practical tools for weather applications.

1 Introduction

Reliable short-term weather forecasts are essential for various applications including crop management, water allocation, flood preparedness, and utility planning. High-resolution weather observations from dense meteorological networks and remote sensing platforms have created new opportunities for statistical modeling of atmosphere-land data. Daily temperature and precipitation fields exhibit substantial variability across spatial scales, are strongly modulated by topography and large-scale circulation, and evolve with seasonal cycles. Forecasting these fields, therefore, requires accounting for joint space-time dependence rather than treating locations or time points independently. Operational weather forecasts are typically based on numerical weather prediction (NWP) models [Bauer et al., 2015], which solve nonlinear differential equations governing atmospheric motion and quantify uncertainty using ensemble simulation. While highly successful, NWP systems demand specialized high-performance computing resources and are not always available at the temporal resolution, geographic domain, or computational budget needed for regional planning, ecological monitoring, or exploratory scientific analysis. In many such settings, statistical models that learn directly from observations offer a valuable complement. Gaussian Process (GP) models provide a flexible, fully probabilistic, and data-driven approach to representing complex space-time structure. In particular, non-separable covariance functions, such as those of Gneiting [2002], allow for spatial correlation to vary with temporal lag and temporal correlation to depend on spatial separation, capturing interactions between space and time that are essential for realistic weather dynamics. These capabilities explain their widespread use in environmental and climate statistics, including weather and short-term spatio-temporal modeling [Cressie and Wikle, 2011, Porcu et al., 2021].

^{*}Institute of Financial Services Zug, Lucerne University of Applied Sciences and Arts

[†]Department of Mathematical Modeling and Machine Learning, University of Zurich

[‡]Seminar for Statistics, ETH Zurich

However, for continental monitoring networks observed over many time points, exact likelihood evaluation and the calculation of predictive distributions for space-time GPs, which requires factorizing an $n \times n$ covariance matrix with $\mathcal{O}(n^3)$ cost and $\mathcal{O}(n^2)$ memory, is computationally infeasible in practice. To make GP models feasible on this scale, a range of approximation strategies have been proposed [see, e.g., Heaton et al., 2019]. Low-rank inducing-point-based approaches such as the modified predictive process approximation, also known as the fully independent training conditional (FITC) approximation, [Quinonero-Candela and Rasmussen, 2005, Banerjee et al., 2008, Finley et al., 2009] capture large-scale spatial and spatio-temporal structure. Local approximations exploit sparsity through covariance tapering [Furrer et al., 2006] or the Vecchia framework [Vecchia, 1988, Datta et al., 2016a, Katzfuss and Guinness, 2021], which induces sparse precision matrices and frequently yields state-of-the-art accuracy in spatial applications [Guinness, 2021, Rambelli and Sigrist, 2025]. Hybrid methods combine these ideas, such as the full-scale approximation [Sang and Huang, 2012] and the Vecchia-inducing-point full-scale (VIF) approximation [Gyger et al., 2025b], where residual dependence is approximated using Vecchia conditioning with correlation-based neighbor search [Kang and Katzfuss, 2023]. Further scalable GP methods include multi-resolution [Katzfuss, 2017] and stochastic partial differential equations-based Lindgren et al. [2011] approximations.

Despite substantial progress on scalable GP approximations, two practical issues become acute in large non-separable space-time applications when working with Vecchia and inducing-points-based approximations: (a) how to construct conditioning sets (neighbors) that remain informative when dependence is not well-described by purely local space-time proximity, and (b) how to place inducing points so that the low-rank structure captures both spatial and temporal variability without manual tuning. In this paper, we address these issues in a unified weather forecasting case study and provide actionable guidance on approximation choices at scale. Our main methodological contributions are the following: (i) a scalable correlation-based neighbor selection strategy for Vecchia approximations with point-referenced data under non-separable space-time dependence, (ii) a space-time separated kMeans++ inducing-point selection algorithm (sts-kMeans++) for pure inducing points methods such as predictive processes and for Vecchia-inducing-point full-scale (VIF) approximations, and (iii) GPU-accelerated implementations of computational bottlenecks enabling efficient estimation and prediction on million-scale space-time datasets.

This paper examines how scalable GP approximations can enable short-term forecasting of temperature and precipitation across the conterminous United States, using observational data rather than physics-based NWP models. Our focus is not on outperforming operational NWP systems, which rely on detailed physical representations of the atmosphere and substantial computational resources, but on assessing how far purely statistical, data-driven GP models can be pushed at continental scale. Such models are relevant in settings where NWP output is unavailable, too coarse in resolution, computationally prohibitive, or impractical to recalibrate for exploratory analysis, uncertainty quantification, or rapid methodological development.

2 Scientific question and dataset

Daily weather conditions at specific locations arise from evolving seasonal cycles, physiographic features, and complex interactions among regional circulation. Consequently, statistical models for weather forecasting must capture dependence not only across large spatial scales but also through time, where local dynamics can change rapidly. This joint space-time structure poses a substantial modeling challenge. While GP models are well-suited for representing such multiscale dependencies, direct GP inference becomes computationally intractable for continental-scale networks with millions of space-time observations. Our focus is therefore on determining whether scalable GP approximations can retain the essential characteristics of space-time dependence, including non-separable interactions between space and time, realistic spatial and temporal correlation ranges, and reliable uncertainty quantification, while making real-time forecasting feasible at continental resolution. Concretely, we treat feasibility as the ability to (i) estimate covariance and mean parameters reliably on large expanding space-time training sets, and (ii) produce well-calibrated predictive distributions with runtimes compatible with routine refitting and forecasting.

To investigate this question, we use an open-source dataset from the National Oceanic and Atmospheric Administration (NOAA) containing daily maximum temperature and precipitation from approximately 3,000 monitoring stations across the conterminous United States. The network ex-

hibits highly heterogeneous spatial coverage - dense in the eastern states and much sparser across the West. Data were retrieved using the R package `rnoaa` (`rnoaa::meteo_pull_monitors`) [Chamberlain et al., 2023] from the Global Historical Climatology Network daily (GHCNd) [Menne et al., 2012]. We analyze 608 consecutive days from 2024-01-01 to 2025-08-31, yielding approximately 1.7 million space-time observations. Figures 5 and 6 in Appendix A show representative snapshots of daily maximum temperature and precipitation amounts across the station network, highlighting the spatial variability present in the dataset. To illustrate the temporal variability and heterogeneity of the observations, Figure 7 in Appendix A displays daily maximum temperature and precipitation for five representative stations spanning contrasting U.S. weather regimes (humid subtropical Miami, arid Phoenix, temperate coastal Seattle, continental Chicago, and high-elevation Denver). Temperatures exhibit pronounced annual seasonality at all locations, with smoother evolution in the West and sharper winter-summer gradients in continental interiors such as Chicago and Denver. In contrast, precipitation is intermittent everywhere but varies strongly in frequency and intensity: Miami and Seattle experience frequent rain events, whereas Phoenix and Denver show long dry spells punctuated by occasional storms. This dataset provides a demanding benchmark: it contains non-Gaussian precipitation responses and strong spatio-temporal residual variation. It therefore offers a realistic testing ground for evaluating the scalability and predictive performance of Vecchia, FITC, and hybrid VIF GP models under a non-separable space-time structure. Importantly, the application spans both a continuous response modeled using a Gaussian likelihood (temperature) and an intermittent, right-skewed response with many zeros (precipitation), allowing us to assess approximation behavior under markedly different distributional regimes. The complete dataset and reproducible code are publicly available at <https://github.com/TimGyger/SpaceTimeGPApprox>.

3 Spatio-temporal Gaussian process model

We model observations at space-time locations $\{(\mathbf{s}_i, t_i)\}_{i=1}^n$, with $\mathbf{s}_i \in \mathcal{S} \subset \mathbb{R}^2$ and $t_i \in \mathcal{T} \subset \mathbb{R}$, as the sum of a structured mean component driven by known geographical, temporal, and climatological covariates, and a random effect that captures residual spatio-temporal variability. The model for the temperature data is

$$\mathbf{Y} = \mathbf{X}\boldsymbol{\beta} + \mathbf{b} + \boldsymbol{\epsilon}, \quad \mathbf{b} \sim \mathcal{N}(\mathbf{0}, \boldsymbol{\Sigma}), \quad \boldsymbol{\epsilon} \sim \mathcal{N}(\mathbf{0}, \sigma^2 \mathbf{I}_n), \quad (1)$$

where $\mathbf{Y} = (Y((\mathbf{s}_1, t_1)), \dots, Y((\mathbf{s}_n, t_n)))^\top \in \mathbb{R}^n$, $\mathbf{X} \in \mathbb{R}^{n \times p}$ is the design matrix constructed from p predictors such as elevation, climate zone, and seasonality, $\boldsymbol{\beta} \in \mathbb{R}^p$ is the corresponding vector of regression coefficients, and $\boldsymbol{\epsilon}$ represents independent microscale variation (a nugget). The latent process \mathbf{b} captures structured space-time dependence with covariance elements $\Sigma_{ij} = c((\mathbf{s}_i, t_i), (\mathbf{s}_j, t_j))$, for a parametric covariance function $c(\cdot, \cdot)$ defined on $\mathcal{S} \times \mathcal{T}$. Constructing valid space-time covariance functions is challenging because they must remain positive definite over both spatial and temporal domains simultaneously. A common simplifying assumption is separability, where $c((\mathbf{s}_i, t_i), (\mathbf{s}_j, t_j)) = c_S(\mathbf{s}_i, \mathbf{s}_j) \cdot c_T(t_i, t_j)$, which decouples spatial and temporal dependence [Gneiting et al., 2006, Chen et al., 2021]. While separability facilitates scalable computation, it prohibits interaction between space and time, which is often unrealistic for weather processes such as moving fronts. To allow for such interactions, Gneiting [2002] propose flexible non-separable covariance functions. A common form [Datta et al., 2016b] is

$$c((\mathbf{s}_i, t_i), (\mathbf{s}_j, t_j)) = \frac{\sigma_1^2 2^{1-\nu}}{\Gamma(\nu)(a|t_i - t_j|^{2\alpha} + 1)^{\delta + \beta d/2}} \left(\frac{c\|\mathbf{s}_i - \mathbf{s}_j\|_2}{(a|t_i - t_j|^{2\alpha} + 1)^{\beta/2}} \right)^\nu K_\nu \left(\frac{c\|\mathbf{s}_i - \mathbf{s}_j\|_2}{(a|t_i - t_j|^{2\alpha} + 1)^{\beta/2}} \right), \quad (2)$$

which reduces to an isotropic Matérn model with smoothness parameter $\nu > 0$ and spatial decay parameter $c > 0$ at zero temporal lag $|t_i - t_j| = 0$. The parameters $\alpha \in (0, 1]$ and $a > 0$ control the smoothness and scaling of the temporal component, respectively, while $\beta \in [0, 1]$ governs the degree of non-separability between space and time, yielding a separable covariance function when $\beta = 0$. The parameter $\delta \geq 0$ further affects the temporal scaling of the overall covariance, independently of the non-separability effect.

As covariates in the fixed effect term, we include spatial coordinates projected into the USGS Contiguous US Albers Equal Area system (*EPSG:5070*, in meters), together with physiographic covariates

capturing large-scale and local terrain effects. These include elevation, distance to the coastline, slope, and terrain orientation, represented through northness and eastness. Nonlinear topographic influences are accommodated by quadratic terms in spatial coordinates and elevation, as well as interactions between elevation, slope, and coastline distance. Seasonal variability is modeled using periodic sine-cosine basis functions at annual and semiannual frequencies. To allow seasonal patterns to vary across space, these basis functions interact with elevation, distance to the coastline, and spatial coordinates, enabling regionally heterogeneous seasonal amplitudes and phases. Large-scale climatological regimes are further represented using Köppen-Geiger climate classifications [Köppen et al., 2011, Beck et al., 2018], obtained via the R package `kgc` [Bryant et al., 2017]. For temperature forecasting, we additionally include 30-year NOAA temperature normals to anchor the mean structure to long-term climatology. Figure 8 in Appendix A illustrates selected covariates.

3.1 Estimation and prediction

We adopt an empirical Bayes approach [Robbins, 1964] and estimate the parameters $\boldsymbol{\theta} = \{\sigma^2, \sigma_1^2, a, c, \alpha, \nu, \beta, \delta\}$ and regression coefficients $\boldsymbol{\beta}$ by maximizing the marginal likelihood. For Gaussian responses, this corresponds to minimizing the negative log-marginal likelihood

$$\mathcal{L}(\boldsymbol{\beta}, \boldsymbol{\theta}; \mathbf{Y}, \mathbf{X}) = \frac{n}{2} \log(2\pi) + \frac{1}{2} \log \det(\tilde{\boldsymbol{\Sigma}}) + \frac{1}{2} (\mathbf{Y} - \mathbf{X}\boldsymbol{\beta})^T \tilde{\boldsymbol{\Sigma}}^{-1} (\mathbf{Y} - \mathbf{X}\boldsymbol{\beta}),$$

where $\tilde{\boldsymbol{\Sigma}} = \boldsymbol{\Sigma} + \sigma^2 \mathbf{I}_n$. Gradients used in gradient-based optimization involve terms such as

$$\frac{\partial}{\partial \boldsymbol{\theta}} \mathcal{L}(\boldsymbol{\beta}, \boldsymbol{\theta}; \mathbf{Y}, \mathbf{X}) = \frac{1}{2} \text{Tr} \left(\tilde{\boldsymbol{\Sigma}}^{-1} \frac{\partial \tilde{\boldsymbol{\Sigma}}}{\partial \boldsymbol{\theta}} \right) - \frac{1}{2} (\mathbf{Y} - \mathbf{X}\boldsymbol{\beta})^T \tilde{\boldsymbol{\Sigma}}^{-1} \frac{\partial \tilde{\boldsymbol{\Sigma}}}{\partial \boldsymbol{\theta}} \tilde{\boldsymbol{\Sigma}}^{-1} (\mathbf{Y} - \mathbf{X}\boldsymbol{\beta}),$$

whose evaluation requires $\mathcal{O}(n^3)$ operations. This motivates the scalable approximations studied in Section 4. The predictive distribution at n_p new space-time points $\{(\mathbf{s}_1^p, t_1^p), \dots, (\mathbf{s}_{n_p}^p, t_{n_p}^p)\}$ is $\mathbf{Y}^p | \mathbf{Y} \sim \mathcal{N}(\boldsymbol{\mu}^p, \boldsymbol{\Sigma}^p)$ with predictive mean $\boldsymbol{\mu}^p = \mathbf{X}^p \boldsymbol{\beta} + \boldsymbol{\Sigma}_{nn_p}^T \tilde{\boldsymbol{\Sigma}}^{-1} (\mathbf{Y} - \mathbf{X}\boldsymbol{\beta})$ and predictive covariance $\boldsymbol{\Sigma}^p = \boldsymbol{\Sigma}_{n_p} + \sigma^2 \mathbf{I}_{n_p} - \boldsymbol{\Sigma}_{nn_p}^T \tilde{\boldsymbol{\Sigma}}^{-1} \boldsymbol{\Sigma}_{nn_p} \in \mathbb{R}^{n_p \times n_p}$, where $\mathbf{X}_i^p = (X((\mathbf{s}_i^p, t_i^p))_1, \dots, X((\mathbf{s}_i^p, t_i^p))_{n_p}) \in \mathbb{R}^{1 \times p}$ is the i -th row of $\mathbf{X}^p \in \mathbb{R}^{n_p \times p}$ containing predictor variables for prediction i , $i = 1, \dots, n_p$, $\boldsymbol{\Sigma}_{nn_p} = [c((\mathbf{s}_i, t_i), (\mathbf{s}_j, t_j))]_{i=1:n_p, j=1:n_p} \in \mathbb{R}^{n_p \times n_p}$ is a cross-covariance matrix, and $\boldsymbol{\Sigma}_{n_p} = [c((\mathbf{s}_i^p, t_i^p), (\mathbf{s}_j^p, t_j^p))]_{i=1:n_p, j=1:n_p} \in \mathbb{R}^{n_p \times n_p}$.

3.2 Extension to non-Gaussian responses for rainfall modeling

Precipitation exhibits a mixed discrete-continuous distribution, with a point mass at zero and a skewed positive tail. Existing approaches either model occurrence and amount separately [Coe and Stern, 1982, Wilks, 1999] or jointly via censored latent-variable models [Bell, 1987, Sansó and Guenni, 2004, Sigrist et al., 2012], following the Tobit framework of Tobin [1958] adapted by Stidd [1973]. We follow this latter approach. Specifically, to model precipitation, we use the likelihood

$$p(\mathbf{Y} | \boldsymbol{\mu}, \sigma^2, \lambda) = \prod_{i=1}^n p(Y((\mathbf{s}_i, t_i)) | \mu((\mathbf{s}_i, t_i)), \sigma^2, \lambda) = \prod_{i=1}^n \left[\Phi \left(-\frac{\mu((\mathbf{s}_i, t_i))}{\sigma} \right) \right]^{\mathbb{1}\{Y((\mathbf{s}_i, t_i))=0\}} \times \left[\frac{1}{\sigma} \phi \left(\frac{Y((\mathbf{s}_i, t_i))^{1/\lambda} - \mu((\mathbf{s}_i, t_i))}{\sigma} \right) \frac{1}{\lambda Y((\mathbf{s}_i, t_i))^{1-1/\lambda}} \right]^{\mathbb{1}\{Y((\mathbf{s}_i, t_i))>0\}},$$

where $\boldsymbol{\mu} = \mathbf{X}\boldsymbol{\beta} + \mathbf{b}$. In such a model, rainfall amounts arise from a censored and power-transformed variable,

$$\mathbf{Y} = \max(\mathbf{0}, \mathbf{X}\boldsymbol{\beta} + \mathbf{b} + \boldsymbol{\epsilon})^\lambda, \quad \mathbf{b} \sim \mathcal{N}(\mathbf{0}, \boldsymbol{\Sigma}), \quad \boldsymbol{\epsilon} \sim \mathcal{N}(\mathbf{0}, \sigma^2 \mathbf{I}_n), \quad (3)$$

where $\lambda > 0$ controls the skewness. The censoring at zero models rainfall occurrence, while the transformation accounts for right-skewed positive amounts and increasing variance at higher intensities. Together, these components define a zero-censored power-transformed normal (ZC-PTN) likelihood, linking precipitation occurrence and intensity through a shared latent GP. As the marginal likelihood is intractable, we use a Laplace approximation [Tierney and Kadane, 1986]; see also Williams and Rasmussen [2006], Sigrist [2023].

4 Approximations and novel methodological contributions

Large-scale spatio-temporal GP models require approximations to remain computationally feasible. Among these, the Vecchia approximations [Vecchia, 1988] have emerged as one of the most accurate and scalable approaches for spatial and spatio-temporal data [Rambelli and Sigrist, 2025], and have been described as a “leader among the sea of approximations” by Guinness [2021].

4.1 Vecchia approximation

Vecchia approximations can be viewed as a structured composite likelihood methods [Varin et al., 2011] in which the full Gaussian likelihood is factorized into a sequence of conditional densities. For a finite-dimensional version of GP $\mathbf{b} = (b((\mathbf{s}_1, t_1)), \dots, b((\mathbf{s}_n, t_n)))^\top$, the exact likelihood factorizes as $p(\mathbf{b} | \boldsymbol{\theta}) = \prod_{i=1}^n p(b((\mathbf{s}_i, t_i)) | b((\mathbf{s}_1, t_1)), \dots, b((\mathbf{s}_{i-1}, t_{i-1})), \boldsymbol{\theta})$. A Vecchia approximation replaces each full conditioning set with a small neighborhood set $N(i)$: $p(\mathbf{b} | \boldsymbol{\theta}) \approx \prod_{i=1}^n p(b((\mathbf{s}_i, t_i)) | \mathbf{b}_{N(i)}, \boldsymbol{\theta})$, where $N(i)$ typically contains the m_v nearest neighbors among the preceding observations. This yields an approximation

$$\mathbf{b} \stackrel{\text{approx}}{\sim} \mathcal{N}(0, \boldsymbol{\Sigma}_s), \quad \boldsymbol{\Sigma}_s = \mathbf{B}^{-1} \mathbf{D} \mathbf{B}^{-T},$$

with a sparse precision matrix $\boldsymbol{\Sigma}_s^{-1} = \mathbf{B}^T \mathbf{D}^{-1} \mathbf{B}$. Here, $\mathbf{B} \in \mathbb{R}^{n \times n}$ is a unit lower-triangular matrix whose nonzero off-diagonal entries in row i occur only in the columns indexed by $N(i)$ and are given by $\mathbf{A}_i = \boldsymbol{\Sigma}_{i, N(i)} \boldsymbol{\Sigma}_{N(i)}^{-1}$, where $\boldsymbol{\Sigma}_{i, N(i)}$ denotes the cross-covariances between $b((\mathbf{s}_i, t_i))$ and its Vecchia neighbors $\{b((\mathbf{s}_k, t_k)) : k \in N(i)\}$, and $\boldsymbol{\Sigma}_{N(i)}$ is the covariance submatrix indexed by $N(i)$. The diagonal matrix $\mathbf{D} = \text{diag}(D_1, \dots, D_n) \in \mathbb{R}^{n \times n}$ is given by $D_i = \boldsymbol{\Sigma}_{i,i} - \mathbf{A}_i \boldsymbol{\Sigma}_{i, N(i)}^T$.

4.2 Low-rank inducing point approximations

A second class of scalable GP methods is based on low-rank approximations constructed from a set of $m \ll n$ inducing points, or knots, $\mathcal{S}_T^* = \{(\mathbf{s}_1^*, t_1^*), \dots, (\mathbf{s}_m^*, t_m^*)\}$. Let $\mathbf{b}^* = (b((\mathbf{s}_1^*, t_1^*)), \dots, b((\mathbf{s}_m^*, t_m^*)))^\top$ denote the latent GP at the inducing points. The predictive process approximation [Banerjee et al., 2008] approximates $b((\mathbf{s}, t)) \approx \mathbf{c}((\mathbf{s}, t), \mathcal{S}_T^*)^\top \boldsymbol{\Sigma}_m^{-1} \mathbf{b}^*$, where $\boldsymbol{\Sigma}_m \in \mathbb{R}^{m \times m}$ is the $m \times m$ covariance matrix of the inducing points and $\mathbf{c}((\mathbf{s}, t), \mathcal{S}_T^*)$ collects their cross-covariances. The implied low-rank covariance is $\boldsymbol{\Sigma}_{mn}^\top \boldsymbol{\Sigma}_m^{-1} \boldsymbol{\Sigma}_{mn}$, where $\boldsymbol{\Sigma}_{mn} \in \mathbb{R}^{m \times n}$ is the cross-covariance matrix between inducing points and observation locations. The fully independent training conditional (FITC) approximation, also known as modified predictive process approximation, [Quinonero-Candela and Rasmussen, 2005, Finley et al., 2009] adds a diagonal variance correction, giving

$$\mathbf{b} \stackrel{\text{approx}}{\sim} \mathcal{N}(0, \boldsymbol{\Sigma}_l), \quad \boldsymbol{\Sigma}_l = \boldsymbol{\Sigma}_{mn}^\top \boldsymbol{\Sigma}_m^{-1} \boldsymbol{\Sigma}_{mn} + \text{diag}(\boldsymbol{\Sigma} - \boldsymbol{\Sigma}_{mn}^\top \boldsymbol{\Sigma}_m^{-1} \boldsymbol{\Sigma}_{mn}).$$

Low-rank approaches capture global structures efficiently, but may struggle to represent fine-scale local variation unless many inducing points are used.

4.3 The Vecchia-inducing-point full-scale (VIF) approximation

VIF approximations introduced in Gyger et al. [2025b] combine the strengths of low-rank and Vecchia methods through a full-scale decomposition. The latent process is decomposed as $b((\mathbf{s}, t)) = b_l((\mathbf{s}, t)) + b_s((\mathbf{s}, t))$, where b_l is a low-rank predictive process capturing large-scale structure and b_s is a residual process capturing local dependence not explained by b_l . The covariance of the low-rank component is $\boldsymbol{\Sigma}_l = \boldsymbol{\Sigma}_{mn}^\top \boldsymbol{\Sigma}_m^{-1} \boldsymbol{\Sigma}_{mn}$, while the residual covariance is $\text{Cov}(\mathbf{b}_s) = \boldsymbol{\Sigma} - \boldsymbol{\Sigma}_{mn}^\top \boldsymbol{\Sigma}_m^{-1} \boldsymbol{\Sigma}_{mn}$. This residual covariance is dense, and it is approximated using a Vecchia approximation $\text{Cov}(\mathbf{b}_s)^{-1} \approx \boldsymbol{\Sigma}_s^{-1} = \mathbf{B}^\top \mathbf{D}^{-1} \mathbf{B}$, where the Vecchia coefficients now use residual covariances adjusted for the low-rank component. Specifically, $D_i = \boldsymbol{\Sigma}_{i,i} - \boldsymbol{\Sigma}_{mi}^\top \boldsymbol{\Sigma}_m^{-1} \boldsymbol{\Sigma}_{mi} - \mathbf{A}_i (\boldsymbol{\Sigma}_{i, N(i)}^\top - \boldsymbol{\Sigma}_{mN(i)}^\top \boldsymbol{\Sigma}_m^{-1} \boldsymbol{\Sigma}_{mi})$, and $\mathbf{A}_i = (\boldsymbol{\Sigma}_{i, N(i)} - \boldsymbol{\Sigma}_{mi}^\top \boldsymbol{\Sigma}_m^{-1} \boldsymbol{\Sigma}_{mN(i)}) (\boldsymbol{\Sigma}_{N(i)} - \boldsymbol{\Sigma}_{mN(i)}^\top \boldsymbol{\Sigma}_m^{-1} \boldsymbol{\Sigma}_{mN(i)})^{-1}$. The resulting full-scale approximation is $\boldsymbol{\Sigma} \approx \boldsymbol{\Sigma}_l + \boldsymbol{\Sigma}_s$.

4.4 Selecting Vecchia neighbors and inducing points

The performance of Vecchia and inducing-points-based GP approximations depends critically on the choice of conditioning sets and inducing point locations. Correlation-based neighbor selection can substantially improve Vecchia accuracy, especially under anisotropy or non-stationarity [Kang and Katzfuss, 2023], but existing approaches are either restricted to gridded data or do not readily extend to general non-separable space-time covariances [Datta et al., 2016b]. For inducing-point methods, common strategies include random subsampling, kMeans++ [Arthur and Vassilvitskii, 2007], and tree-based approaches [Terenin et al., 2022], with kMeans++ offering a favorable accuracy-cost trade-off in spatial FITC and full-scale settings [Gyger et al., 2025a]. Extending such strategies to non-separable space-time models, particularly for forecasting, remains an open challenge.

4.4.1 Correlation-based Vecchia neighbor selection

Classical Vecchia approximations select neighbors via Euclidean distances, but Kang and Katzfuss [2023] demonstrate that correlation-based searches often yield higher accuracy. Depending on the covariance structure, this may reduce to Euclidean distance after an appropriate coordinate transformation. In our setting, however, neither the Gneiting covariance (2) nor the residual covariance used in VIF admits such transformations. For the VIF residual process with covariance $\Sigma - \Sigma_{mn}^T \Sigma_m^{-1} \Sigma_{mn}$, Gyger et al. [2025b] propose using the correlation distance $\rho_r((\mathbf{s}_i, t_i), (\mathbf{s}_j, t_j)) = [\Sigma]_{ij} - \Sigma_{mi}^T \Sigma_m^{-1} \Sigma_{mj}$, yielding the metric

$$d_r((\mathbf{s}_i, t_i), (\mathbf{s}_j, t_j)) = \sqrt{1 - \left| \frac{\rho_r((\mathbf{s}_i, t_i), (\mathbf{s}_j, t_j))}{\sqrt{\rho_r((\mathbf{s}_i, t_i), (\mathbf{s}_i, t_i)) \rho_r((\mathbf{s}_j, t_j), (\mathbf{s}_j, t_j))}} \right|}.$$

For standalone Vecchia approximations, the analogous correlation metric is

$$d_c((\mathbf{s}_i, t_i), (\mathbf{s}_j, t_j)) = \sqrt{1 - \left| \frac{[\Sigma]_{ij}}{\sqrt{[\Sigma]_{ii} [\Sigma]_{jj}}} \right|}.$$

Nearest-neighbor search with respect to both correlation metrics can be implemented efficiently using cover trees [Beygelzimer et al., 2006]. We use an extension of the cover tree algorithm to enable efficient correlation-based neighbor selection for general, non-separable space-time covariance functions. In contrast to standard constructions that randomly select candidate nodes during tree building, we insert points sequentially according to their index order, following the procedure outlined in Algorithm 2 in Appendix B. This modification restricts candidate neighbors to observations with smaller indices, which is consistent with the Vecchia factorization and simplifies the neighbor search, leading to improved runtime performance, see Algorithm 3 in Appendix B for more details. Because covariance parameters evolve during likelihood optimization, neighbor sets are updated at optimization iterations indexed by powers of two and once more upon convergence. If an update alters the likelihood, optimization is resumed until convergence is achieved.

Moreover, a Vecchia approximation depends on the ordering of observations, since each conditional density is formed using only a subset of previously ordered points. Proposed strategies include simple coordinate-based orderings, maximum-minimum (max-min), and random orderings [Guinness, 2018]. For space-time data, however, the problem becomes more delicate: ordering solely by spatial coordinates can lead to conditioning sets drawn from irrelevant times, whereas ordering only by time may overlook essential spatial structure within each snapshot. Idir et al. [2025] systematically compared ordering schemes for space-time Vecchia approximations and found that random ordering and max-min ordering generally provided the best accuracy. Motivated by these results and the computational efficiency of a random ordering, we adopt a hybrid scheme: observations are ordered by time to preserve temporal causality, with random spatial ordering within each time point.

4.4.2 Space-time separated kMeans++ algorithm for inducing points selection

For non-separable space-time covariance functions such as the one in (2), spatial and temporal correlations may each be strong while their joint dependence decays quickly. As a result, if clustering is applied directly in the full space-time domain, inducing points can be selected that are near in space

and time yet weakly correlated when considered jointly, leading to an inefficient low-rank representation. This is particularly relevant for weather forecasting, where the main objective is short lead time prediction, often at locations with sparse or no observational history. In such settings, inducing points are unlikely to be time-wise close to the prediction sites, and forecast accuracy depends critically on how well the temporal evolution of the field is represented. Thus, capturing temporal structure can be more influential than maximizing the domain coverage of inducing points. To address this, we propose a space-time separated kMeans++ (sts-kMeans++) inducing-point selection strategy: spatial and temporal centers are selected independently via kMeans++, and their Cartesian product defines a structured but irregular grid. This approach yields inducing points that may share locations at multiple times (enhancing temporal representation) and occupy distinct locations at a single time point (preserving spatial support). The numbers of spatial and temporal centers, m_s and m_t , are chosen proportional to the number of unique time points and the average number of stations per time; see Algorithm 1. The resulting method has computational cost $\mathcal{O}(n(m_s + m_t))$. Figure 9 in Appendix B visualizes the joint and sts-kMeans++ inducing point selection.

Algorithm 1 Space-time separated kMeans++ inducing points

Input: Data $\mathcal{D} = \{(\mathbf{s}_1, t_1), \dots, (\mathbf{s}_n, t_n)\} \subset \mathcal{S} \times \mathcal{T}$ with \mathcal{T} the set of unique time points and \mathcal{S} the set of unique space points, total inducing points m
Output: $\mathcal{S}_{\mathcal{T}}^* = \{(\mathbf{s}_1^*, t_1^*), \dots, (\mathbf{s}_{\hat{m}}^*, t_{\hat{m}}^*)\}$ with $\hat{m} \approx m$

- 1: $m_s \leftarrow \text{round}(\sqrt{\frac{mn}{|\mathcal{T}|^2}})$, $m_t \leftarrow \text{round}(\sqrt{\frac{m|\mathcal{T}|^2}{n}})$ $\triangleright \hat{m} = m_s \cdot m_t \approx m$
- 2: $\bar{\mathcal{T}} \leftarrow \text{kMeans++}(\mathcal{T}, m_t)$, $\bar{\mathcal{S}} \leftarrow \text{kMeans++}(\mathcal{S}, m_s)$
- 3: $\mathcal{S}_{\mathcal{T}}^* \leftarrow \{(\mathbf{s}, t) | (\mathbf{s}, t) \in \bar{\mathcal{S}} \times \bar{\mathcal{T}}\}$

4.5 GPU acceleration

Gaussian process computations rely heavily on repeated matrix multiplications, linear solves, and neighbor searches. Even with Vecchia and low-rank approximations, these operations remain the main computational bottlenecks for large space-time datasets, motivating targeted acceleration. Modern platforms combine CPUs and GPUs, whose complementary architectures are well suited to this workload. In this work, we accelerate the dominant computations by offloading dense linear algebra involving cross-covariance matrices (e.g., products and solves with Σ_{mn} and Σ_m), sparse matrix–matrix multiplications involving the Vecchia factors \mathbf{B} and \mathbf{D} , and Vecchia neighbor searches to the GPU. All methods are implemented in the `GPBoost` software library using optimized NVIDIA CUDA routines, including cuBLAS, cuSPARSE, and cuSOLVER. Currently, GPU support for the Gneiting (2) and Matérn covariance is provided for smoothness values $\nu \in \{0.5, 1.5, 2.5\}$, for which these kernels admit closed-form expressions involving only elementary functions, thereby avoiding the need to evaluate the modified Bessel function K_ν on the GPU. The remaining sequential or low-dimensional computations are handled on the CPU. This hybrid approach enables substantial speedups without rewriting the full code base, while preserving portability and reproducibility. Note that calculating the matrices \mathbf{B} and \mathbf{D} in Vecchia approximations on the GPU did not result in a speed-up compared to the CPU-based Vecchia implementation in the `GPBoost` library.

5 Simulated experiments

We first compare the predictive and inferential performance of the above-introduced GP approximations using simulated experiments. Specifically, we evaluate Vecchia approximations with either Euclidean or correlation-based nearest-neighbor selection, both using $m_v = 30$ neighbors. For low-rank inducing-point methods, we consider FITC approximations with inducing points selected via both the standard kMeans++ and the proposed sts-kMeans++ algorithm, in both cases using $m = 500$ inducing points. Finally, we evaluate the hybrid VIF approximation, which combines correlation-based Vecchia neighbor selection with sts-kMeans++-selected inducing points, using $m_v = 30$ and $m = 500$. All experiments are conducted on a system equipped with an AMD EPYC 7763 processor using 16 CPU threads, 512 GB of system memory, and an NVIDIA L40S GPU with 48 GB of VRAM. GPU-based computations refer to executions that utilize the L40S GPU in addition to the CPU, whereas CPU-based computations are performed exclusively on the AMD EPYC 7763 processor. All methods are

implemented using **GPBoost**, and the complete **R** and **Python** source code and datasets required to reproduce the experiments are publicly available at <https://github.com/TimGyger/SpaceTimeGPAprox>.

First, we generate 10 zero-mean spatio-temporal GP samples of size 15,000 using the non-separable covariance (2) with nugget $\sigma^2 = 0.01$ and parameters $(\sigma_1^2, a, c, \alpha, \nu, \beta, \delta) = (1, 0.5, 20, 0.4, 1.5, 0.4, 0.2)$. A total of 500 spatial locations are sampled uniformly over $[0, 1]^2$ and observed at 30 equally spaced time points; see Appendix C for an illustration. Observations with $t \leq 20$ form the training set ($n = 10,000$), and those with $t > 20$ form the test set ($n_p = 5,000$). Parameters are estimated by maximizing the marginal likelihood using the limited-memory BFGS algorithm. Predictive performance is evaluated using the RMSE and the continuous ranked probability score (CRPS) given by $-\frac{1}{n_p} \sum_{i=1}^{n_p} \sigma_i^p \left(\frac{1}{\sqrt{\pi}} - 2 \cdot \phi\left(\frac{y_i^* - \mu_i^p}{\sigma_i^p}\right) - \frac{y_i^* - \mu_i^p}{\sigma_i^p} (2 \cdot \Phi\left(\frac{y_i^* - \mu_i^p}{\sigma_i^p}\right) - 1) \right)$ for Gaussian likelihoods, where $\phi(x) = \frac{1}{\sqrt{2\pi}} \exp\left(-\frac{x^2}{2}\right)$ and $\Phi(x)$ are the density and cumulative distribution functions (CDFs), respectively, of a standard normal distribution, y^* is the test response, and μ^p and σ^p are the predictive means and variances, respectively. Figure 1 summarizes the RMSE and CRPS across different lead times. The results show that the correlation-based neighbor selection leads to a clear accuracy gain for the Vecchia approximation, yielding uniformly lower errors than Euclidean-based neighbors at every forecast horizon. For the FITC approximation, choosing inducing points via the proposed sts-kMeans++ procedure consistently improves the prediction accuracy relative to kMeans++. Across all settings, the VIF approximation provides the most accurate predictions and the most stable uncertainty quantification, outperforming both standalone Vecchia and FITC approaches. Figure 11 in Appendix C compares estimated parameters to their true values. The Vecchia approximation with Euclidean neighbors struggles to identify the temporal smoothness (α), whereas the Vecchia approximation with a correlation-based neighbor selection and the VIF approximation yield accurate estimates for all covariance parameters. The FITC approximation exhibits marked biases, especially in the nugget parameter, indicating difficulty in capturing fine-scale variability.

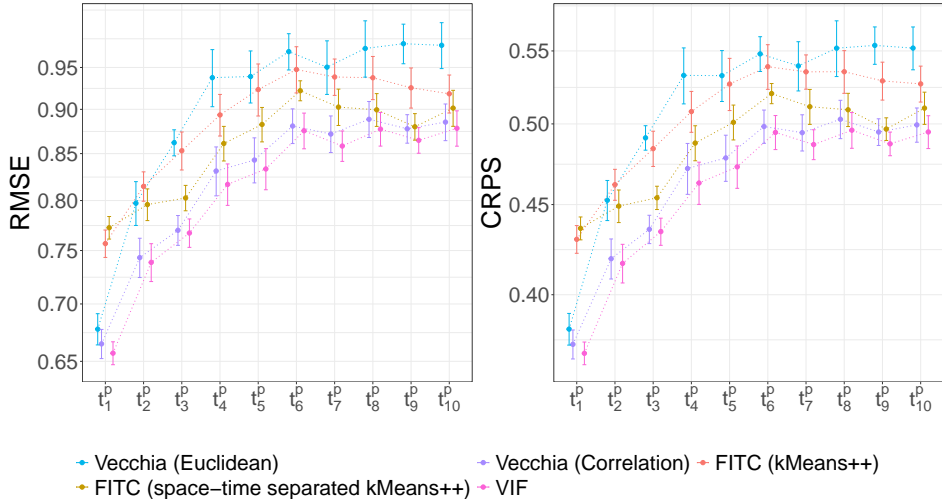


Figure 1: Average RMSE and CRPS (log scale) \pm one standard error vs. lead time for the Vecchia, FITC, and VIF approximations.

To assess performance at realistic scales, we apply all methods to the synthetic benchmarks from the Second Spatial Statistics Competition 2a and 2b [Abdulah et al., 2022], which provide exact GP samples from the Gneiting covariance function (2). The datasets contain 100,000 and 1,000,000 observations, respectively, with 100 time points and up to 10,000 spatial locations per time point. Using these benchmarks avoids cubic simulation costs and enables direct comparison with exact methods such as *ExaGeoStat* [Abdulah et al., 2018]. We consider three regimes of space-time dependence (strong, moderate, and weak), defined by different covariance parameter settings. The corresponding parameter values and effective spatial and temporal ranges are reported in Table 4 in Appendix D. We consider three prediction tasks, namely withheld spatial locations (RS), withheld space time locations (RST), and temporal extrapolation (T10), using 90% of the data for training and RMSE for evaluation. The results for sub-competition 2a reported in Table 1 show that the VIF and Vecchia with correlation-

based neighbor selection approximations consistently achieve RMSE values close to the exact model across all scenarios, whereas Euclidean neighbor selection is less accurate under rapidly decaying dependence. FITC approximations perform poorly in interpolation settings but become competitive for temporal extrapolation, particularly when using sts-kMeans++ for selecting inducing points. This highlights the importance of targeted temporal coverage when forecasting beyond the observation window, where spatial proximity to inducing points is limited.

RMSE		Vecchia Euc.	Vecchia Corr.	FITC kMeans++	FITC sts-kMeans++	VIF	ExaGeoStat
RS	\mathcal{D}_1	0.707073	0.701579	0.888506	0.888751	0.700932	0.696989
	\mathcal{D}_2	0.227223	0.227249	0.816669	0.907848	0.227232	0.227171
	\mathcal{D}_3	0.046763	0.046765	0.333600	0.700298	0.046770	0.046780
RST	\mathcal{D}_1	0.708225	0.615680	0.894176	0.888547	0.615148	0.610297
	\mathcal{D}_2	0.222245	0.222248	0.805316	0.889083	0.222247	0.221473
	\mathcal{D}_3	0.046240	0.046239	0.354850	0.703996	0.046239	0.040588
T10	\mathcal{D}_1	0.923049	0.904621	0.926686	0.918036	0.904412	0.901485
	\mathcal{D}_2	0.939343	0.938799	0.962824	0.937738	0.938799	0.932938
	\mathcal{D}_3	0.913873	0.913874	0.751174	0.744102	0.909280	0.777060

Table 1: RMSE for sub-competition $\mathcal{Q}a$ [Abdulah et al., 2022]; last column from Tables S4–S6.

Table 5 in Appendix D reports the RMSE of the VIF approximation across all datasets and scenarios in sub-competition $\mathcal{Q}b$ [Abdulah et al., 2022], compared with the four top competitors.

5.1 GPU acceleration

Next, we analyze the speedup provided by GPU acceleration. Figure 2 reports runtimes and speedups for a single optimization iteration (two likelihood evaluations, gradient computation, and two Vecchia neighbor searches) across varying sample sizes and for different approximation methods. GPU acceleration yields substantial gains, particularly for methods with correlation-based neighbor searches (Vecchia and VIF). For instance, GPU acceleration provides a speedup of a factor of close to 20 for the correlation-based Vecchia approximation for a sample size of 1,000,000. FITC and VIF approximations also benefit from GPU acceleration due to matrix multiplications involving Σ_{mn} . Furthermore, Table 6 in Appendix E reports runtimes for the sub-competition $\mathcal{Q}b$ of Abdulah et al. [2022], with and without GPU acceleration. The resulting speedups are consistent with those observed in Figure 2.

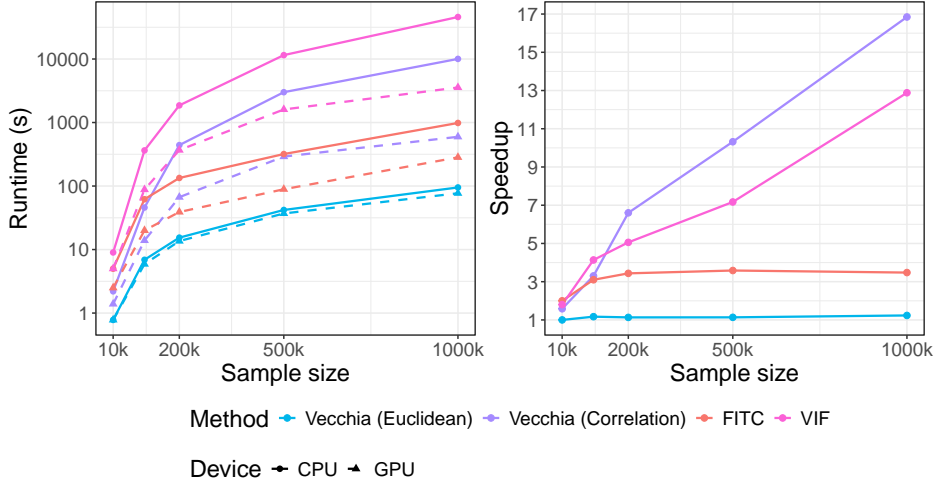


Figure 2: Runtimes in seconds (log-scale) and GPU speedups per optimization step across sample sizes for the Vecchia, FITC, and VIF approximations.

Additional experiments in Appendix E confirm these findings for more general GP settings, including non-Gaussian likelihoods fitted via Laplace approximation and high-dimensional inputs with automatic relevance determination (ARD) Matérn kernels. In all cases, GPU acceleration substantially reduces runtime, with the largest gains when neighbor search dominates. In the ARD experiments (Figure 14), speedups increase with dimension due to the growing cost of distance computations.

These results show that GPU acceleration enables scalable GP inference beyond space-time modeling, including high-dimensional regression settings, without requiring any changes to the end user’s workflow.

6 Application to short-term weather prediction

In the following, we apply the proposed methodology to generating short-term forecasts of daily maximum temperature and precipitation across the conterminous United States using the datasets and models described in Sections 2 and 3, respectively. The observational network comprises 3,057 stations with highly heterogeneous spatial coverage (see Figures 5 and 6 in Appendix A). Such variability directly motivates scalable space-time modeling, as accurate prediction must transfer information across regions with widely differing station density. The dataset contains 608 consecutive days from 2024-01-01 to 2025-08-31. Forecasts are produced using an expanding-window framework. All observations from 2024 serve as the initial training set. This initial training dataset contains more than one million space-time observations. Beginning on January 1, 2025, we sequentially generate forecasts on every day for daily temperatures and rainfall with lead times of five and three days, respectively. The covariance parameters are re-estimated at the end of each month which allows for adapting to temporal non-stationarity (e.g., seasonal shifts in variability and correlation structure). Compared to a daily re-estimation, this reduces computation times while retaining operational realism. We use the same computational environment including GPU acceleration and the same number of Vecchia neighbors and inducing points as in Section 5.

To evaluate prediction accuracy, a random subset of approximately 25% of the stations is withheld entirely during training. This spatio-temporal test data design ensures that every model is evaluated not only for temporal forecasting at observed sites but also for its ability to transfer information to previously unmonitored locations. In practice, forecast users often require predictions in areas with sparse observational histories, at newly installed sensors, or in regions without any monitoring infrastructure (e.g., agricultural zones, remote mountain terrain, coastal transition areas). The Python code used to run all experiments is publicly accessible at <https://github.com/TimGyger/SpaceTimeGPAprox>.

6.1 Short-term prediction of daily maximum temperature

Daily maximum temperature is modeled using the model in (1) with the space-time covariance function given in (2). We fix the Matérn smoothness parameter to $\nu = 1.5$. Estimating ν on a GPU is currently not implemented, but estimating it on subsets of the data using CPU gives $\nu \approx 1.5$ (results not tabulated). The model is fitted using the scalable approximation strategies introduced in Section 4. We generate rolling one- to five-day-ahead forecasts throughout 2025 and compare the GP-based approaches with two non-GP baselines: a simple persistence forecast using the previous day’s maximum temperature and a fixed-effects linear regression model without a GP.

Figure 3 summarizes the forecast performance for spatio-temporal prediction using the RMSE and CRPS. Across all prediction horizons, a correlation-based neighbor selection improves the Vecchia approximation relative to Euclidean-distance-based neighbors, and the FITC approximation is highly sensitive to the inducing points placement. In particular, the proposed sts-kMeans++ strategy substantially enhances the FITC approximation’s accuracy compared with standard kMeans++. The VIF approximation, which uses the sts-kMeans++ method for selecting inducing points and correlation-based Vecchia neighbor selection, yields the best overall performance, achieving slightly lower errors than the correlation-based Vecchia approximation across all lead times. Regarding the benchmarks, both VIF and correlation-based Vecchia clearly outperform the persistence and the fixed-effects linear model at every horizon. This highlights the value of explicitly modeling space-time dependence even in very short-range forecasting, where relying solely on past observations or covariates is insufficient. In Figure 15 in Appendix F, we report additional results also evaluating the models for temporal-only predictions at stations for which data has been observed. These results are qualitatively very similar to the space-time prediction results. Table 7 in Appendix E reports the overall RMSE and CRPS aggregated across the full five-day horizon for pure temporal, and spatio-temporal, together with average computation times. The VIF approximation provides the highest prediction accuracy, albeit at a higher training cost than the Vecchia methods. The FITC approximation is computationally inexpensive but substantially less accurate. Across all scalable approximations, forecast generation is

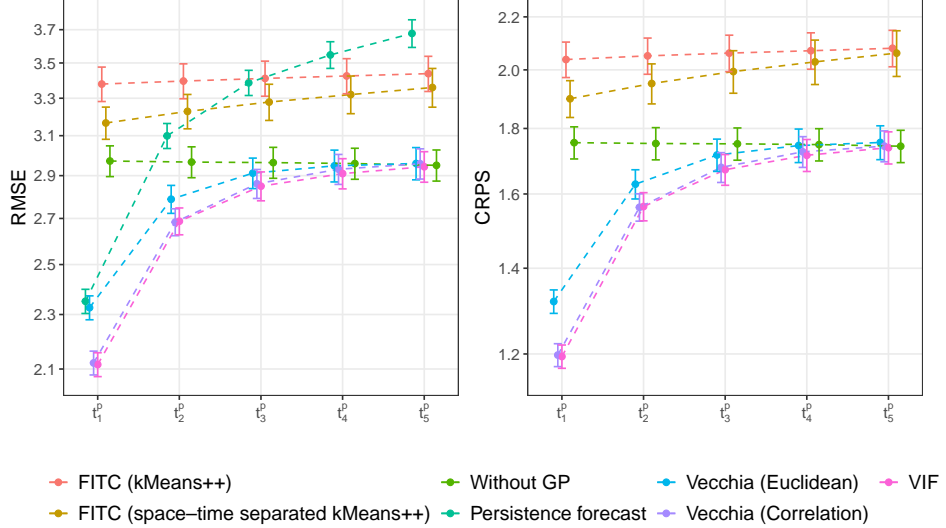


Figure 3: Temperature modeling results: average RMSE and CRPS (log scale) \pm one standard error vs. lead time (days) for one- to five-day spatio-temporal forecasts using the Vecchia, FITC, and VIF approximations. Persistence and fixed-effects-only baselines are included.

inexpensive: computing predictive means and variances requires only a few tens of seconds. Thus, the dominant computational expense arises from parameter estimation rather than daily forecasting. Even for the most accurate method (VIF), a full re-estimation takes on the order of one hour, while the Vecchia variants complete training within minutes. These runtimes remain practical even without GPU acceleration. Even on standard CPU hardware, monthly parameter re-estimation can be performed offline (e.g., overnight) after which operational 5-day forecasts can be issued almost instantly. Consequently, scalable GP models can be deployed in routine forecasting workflows without specialized hardware, while still delivering high-accuracy, uncertainty-aware predictions at continental scale.

Figure 16 in Appendix F displays the forecast error for the VIF approximation throughout 2025. The accuracy improves over time as additional data accumulate, with notably strong performance in late summer, when temperature fields evolve more smoothly than in winter and spring. Furthermore, spatial variation in the station-wise averaged one-day-ahead forecast accuracy is shown in Figure 18 in Appendix F for August 2025. The FITC approximations, particularly with standard kMeans++ inducing points, perform uniformly worse than the other methods across all regions. In contrast, differences between the VIF approximation and the Vecchia methods (with either Euclidean or correlation-based neighbor selection) are visually small. For the VIF and Vecchia approaches, errors are lowest throughout the Southeast, where summer temperature fields vary smoothly and station density is high. Higher errors occur in regions with strong synoptic variability or complex terrain, including the northern Rockies, the Upper Midwest, and portions of the Northeast, where sharp frontal transitions and local land-atmosphere interactions lead to more abrupt temperature changes. Figure 17 in Appendix F displays one-day-ahead temperature residuals under the VIF approximation for selected stations. The residuals show no systematic drift over the year, indicating that the VIF-approximated GP model successfully captures both the seasonal cycle and short-lead temperature dynamics. Residual magnitudes vary across stations, reflecting local variability in daily temperature fluctuations, but no persistent patterns of under- or over-prediction are evident. In addition, we check calibration of the forecasts using the probability integral transform (PIT). Uniform(0,1) QQ-plots of PIT transformed values shown in Figure 20 in Appendix F.1 indicate that the VIF and the two Vecchia approximations generate well calibrated forecasts for all lead times, while the FITC approximations show noticeably poorer calibration.

Table 2 reports the covariance parameters estimated by the VIF model at the estimation in late July 2025; the full sequence of monthly estimates is provided in Table 8 in Appendix F. The spatial and temporal effective ranges remain remarkably stable across months, indicating that short-lead temperature forecasts are governed by persistent large-scale dependence rather than rapid structural changes.

Such parameter stability is desirable in practice, as it implies that models need not be re-tuned frequently to maintain forecasting skill. The July estimates show a spatial effective range of roughly 1,400 km, reflecting broad continental-scale coherence in daily maximum temperatures, and a temporal range of about seven days, consistent with the lifespan of synoptic systems. The non-separability parameter ($\beta \approx 1$) suggests strong space-time interaction, in line with slowly evolving air-mass advection that shapes temperature dynamics across much of the United States. Figure 19 in Appendix F displays the estimated GP random effects across the conterminous United States for several temporal lags, illustrating how each approximation captures the underlying spatial and temporal dependence structure.

σ^2	σ_1^2	a	$c \cdot 10^5$	α	β	δ	Time range	Space range
1.539	6.193	0.090	0.337	0.831	0.999	1.667	6.7 days	1,408 km

Table 2: VIF covariance estimates (July); ranges defined by correlation decay to 0.05.

To assess potential spatial non-stationarity in the covariance structure, we re-estimated the VIF model at the final recalibration date on three broad geographic subsets (West, Central, East). The resulting parameter estimates for the Central and Eastern subsets are very similar to those obtained from the full dataset (results not tabulated). Spatial effective ranges varied only modestly, from about 1,477 km to 1,597 km, slightly bigger than the full-domain estimate, while temporal effective ranges remained between 8.6 and 11 days. The estimated non-separability parameter was also close to $\beta \approx 1$ in both regions. In contrast, the Western subset exhibited a noticeably larger spatial effective range together with a reduced non-separability parameter, reflecting the broader-scale temperature coherence and weaker space-time coupling over the western United States. Overall, stationarity appears adequate at the continental scale, with only moderate regional deviations.

6.2 Short-term prediction of precipitation

For precipitation, we use the covariance structure (2) with the Matérn smoothness fixed to $\nu = 0.5$. This corresponds to an exponential covariance, producing a rougher latent process that more realistically captures the sharp spatial and temporal variability characteristic of rainfall. Estimating the smoothness parameter using only CPU on subsets of the data gives $\nu \approx 0.5$. Daily precipitation exhibits a mixed distribution with a discrete component (occurrence) and a continuous component (amount). To account for this, we use the zero-censored power-transformed normal (ZC-PTN) likelihood introduced in (3) in Section 3.2. A Laplace approximation is used for parameter estimation and prediction. To reduce the computational complexity, we employ the iterative and stochastic techniques of Kündig and Sigrist [2025] and Gyger et al. [2025b], which replace explicit matrix factorizations with iterative methods that only require matrix-vector operations. To evaluate the predictive accuracy, we use separate metrics for occurrences and intensities. Because skill in precipitation forecasting deteriorates more rapidly with lead time than for temperature, we focus on one- to three-day-ahead forecasts, an operationally relevant horizon at which meaningful predictability can still be obtained. We also examined up to five-day-ahead forecasts; however, accuracy remained largely similar or only slightly degraded. For rainfall occurrence, we use the Brier score (BS) and the log score (LS), which assess both sharpness and calibration of the implied occurrence probabilities. Conditional on rainfall occurrence, positive-amount predictions are evaluated using the mean absolute error (MAE), which is interpretable on the original scale and robust to the heavy right tail of precipitation amounts. To assess probabilistic predictions, we additionally consider the continuous ranked probability score (CRPS), computed by sampling from the ZC-PTN predictive distributions. All GP-based methods are compared with a fixed-effects linear regression model without a GP and a simple persistence benchmark based on the previous day’s precipitation occurrence and amount.

Figure 4 reports the accuracy measures for precipitation amounts (MAE, CRPS) and occurrences (BS, LS) versus lead times. Table 9 in Appendix F additionally reports average accuracy measures over all prediction horizons and days as well as runtimes. Concerning precipitation amounts, we first observe that the correlation-based neighbor selection improves the Vecchia approximation for one-day ahead forecasts. As in the temperature application, the FITC approximation is sensitive to the inducing-point placement, with the proposed sts-kMeans++ strategy substantially outperforming standard kMeans++. The VIF approximation achieves the lowest CRPS across all horizons and all

metrics. Moreover, the persistence forecast performs consistently inferior to the GP approximations, underscoring both the value of relevant covariates and the importance of explicitly modeling space-time dependence in short-term precipitation forecasting. Concerning the fixed-effects linear regression model without a GP component, both the VIF and Vecchia approximations yield superior performance. As shown in Figure 21 in Appendix F, the gap between temporal and spatio-temporal forecasting is slightly larger for precipitation than for temperature, yet still remains very modest. This is noteworthy given the inherently localized and rapidly evolving nature of rainfall. Convective storms, orographic lifting, and frontal passages should, in principle, make prediction at unobserved stations substantially more difficult. The relatively small deterioration in skill suggests that the GP models capture the relevant fine-scale spatial structure and, together with the covariates, effectively propagate information to new locations through their joint space-time covariance.

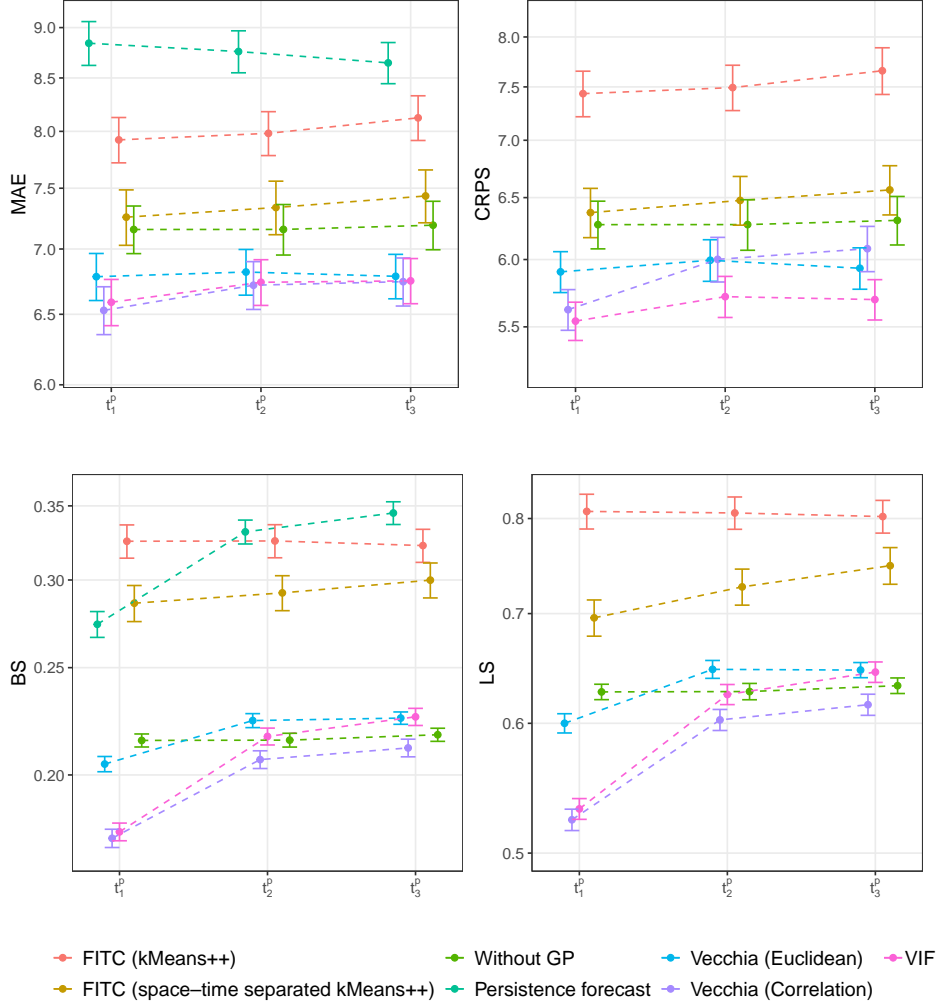


Figure 4: Precipitation modeling results: Average MAE and CRPS for precipitation amounts and brier score (BS) and log score (LS) for precipitation occurrence (log scale) \pm one standard error vs. lead time (days) for one- to three-day spatio-temporal forecasts using the Vecchia, FITC, and VIF approximations. Persistence and fixed-effects-only baselines are included.

For precipitation occurrence, we find that a Vecchia approximation with correlation-based neighbor selection consistently outperforms its Euclidean-based counterpart. The improvements are most pronounced at short horizons, where the correlation-based Vecchia and VIF approximations yield the lowest BS and LS. Within the FITC family, the choice of inducing-point placement has a modest effect, although the proposed sts-kMeans++ strategy offers better performance than standard kMeans++. Nonetheless, both FITC variants remain inferior to the other GP approximations, reflecting their

difficulty in capturing highly localized, rapidly evolving precipitation processes. While persistence forecasts perform reasonably well at short lead times, the best GP-based models consistently achieve superior predictive accuracy. Moreover, for one-day-ahead forecasts, both the VIF and correlation-based Vecchia approximations clearly outperform the fixed-effects linear regression model without a GP component. As shown in Figure 22 in Appendix F, the performance gap between temporal and spatio-temporal forecasting is again almost negligible for rainfall occurrence. As a result, GP models can transfer occurrence information from monitored to unmonitored stations with little accuracy loss. For comparison, Figure 22 in Appendix F also reports results for a latent GP model with a Bernoulli likelihood and a logit link function. Unlike the ZC-PTN model, this model only uses binary wet/dry data and ignores precipitation amounts. However, we observe only minor differences compared to the ZC-PTN likelihood for the most accurate GP models (a correlation-based Vecchia approximation and a VIF approximation).

Compared to a Gaussian likelihood used for temperature modeling, we observe higher runtimes for all methods for the non-Gaussian ZC-PTN likelihood. Nonetheless, even the most accurate model (VIF) remains computationally feasible: estimation takes on the order of a few hours, while the cheaper Vecchia variants require only tens of minutes. As in the Gaussian case, prediction remains inexpensive (tens of seconds), meaning that computational cost lies almost exclusively in model fitting rather than forecasting.

Spatial variability in the averaged station-wise one-day-ahead forecast accuracy is shown in Figure 23 in Appendix F for August 2025. The benefits of correlation-based Vecchia neighbor selection are most evident in the CRPS and BS fields, where it yields lower error patterns than Euclidean neighbors, particularly in the middle and eastern parts of the country. For the VIF and Vecchia approaches, forecast errors generally increase from west to east. Much of the western United States experiences dry, spatially smooth summer conditions, which are easier to model and, therefore, yield lower uncertainty. In contrast, the eastern half of the country, particularly the Southeast and the Mid-Atlantic, exhibits frequent, localized rainfall driven by convective storms, tropical moisture intrusions, and frontal boundaries, making both occurrence and intensity harder to predict. Higher errors also appear across the Central and Upper Midwest (including states such as Iowa, Minnesota, and Missouri). This region sits along common summertime storm tracks and is strongly influenced by mesoscale convective systems that can produce large rainfall gradients over short distances. These systems evolve rapidly overnight and propagate long distances, introducing substantial spatial and temporal variability that challenges short-term prediction, especially at unobserved stations. Station-level one-day-ahead precipitation residuals reported in Figure 24 in Appendix F show a tendency to underestimate rainfall amounts for larger events. This pattern is consistent with the challenges of predicting convective and storm-driven extremes at daily resolution. Regions dominated by frequent, moderate-intensity rainfall exhibit more balanced residuals, whereas areas with highly intermittent or topographically forced precipitation show larger conditional errors. Occurrence residuals remain centered near zero, with a mild tendency to underpredict rainy days. This reflects the difficulty of anticipating rare or localized precipitation events, while periods with more regular rainfall yield smaller occurrence errors. Overall, the lack of sustained bias in either component indicates stable performance of the GP model across diverse precipitation regimes. In Figure 26 in Appendix F.2, we additionally report randomized PIT reliability diagrams to assess calibration. We find that the FITC and Euclidean-based Vecchia approximations are not well calibrated, having a systematic downward bias. The VIF and correlation-based Vecchia approximations are much better calibrated, but still exhibit a small downward bias.

Table 3 reports the covariance parameters estimated by the VIF model at the end of July 2025. Across all monthly re-estimations reported in Table 10 in Appendix F, the parameters remain stable, indicating that the large-scale space-time dependence structure of precipitation is persistent over the year, with only modest seasonal adjustments. Between January and July 2025, the temporal effective range increases slightly (3.3 to 3.7 days), while the spatial range decreases (3,300 km to 2,770 km), reflecting the transition from winter's broad synoptic precipitation to more localized warm-season convection. The non-separability parameter increases only marginally (0.26 to 0.265), implying that the overall strength of space-time interaction remains essentially unchanged. In comparison with the temperature application, the precipitation model exhibits both a shorter temporal range and weaker non-separability, underscoring the fundamentally faster and more localized dynamics of precipitation. The power-transformation parameter λ also increases modestly, consistent with heavier-tailed rainfall amounts during the warm season. Figure 25 in Appendix F shows the estimated GP random effects

over the conterminous United States at multiple temporal lags, providing a visual comparison of how the different approximations represent space-time dependence. To further assess potential spatial non-stationarity in the covariance structure, we re-estimated the VIF model at the final recalibration date on three geographic subsets: West, Central, and East. The resulting parameter estimates (results not tabulated) were highly similar to those obtained from the full dataset. Spatial effective ranges varied only modestly - from about 2,463 km to 2,627 km, slightly smaller than the full-domain estimate - while temporal effective ranges remained between 3.6 and 3.9 days. The estimated non-separability parameter was stable across all subsets, with $\beta \approx 0.26$ in each case. These findings suggest no evidence of large-scale spatial non-stationarity.

σ	λ	σ_1^2	a	$c \cdot 10^5$	α	β	δ	Time range	Space range
3.415	1.508	18.286	0.230	0.108	0.860	0.265	2.353	3.7 days	2,774 km

Table 3: VIF auxiliary and covariance estimates (July), and resulting ranges.

7 Conclusion

This study demonstrates that scalable Gaussian Process (GP) models can deliver accurate short-term forecasts of temperature and precipitation across the continental United States while remaining computationally feasible at operational scale. Using a nonseparable space-time covariance, the models capture realistic weather dependence, with spatial correlation varying across both time lags and regions. Two methodological advances underpin this performance: a scalable correlation-based Vecchia neighbor selection method and the sts-kMeans++ method for selecting inducing points. Together, these ideas are integrated into the VIF approximation, which provides the strongest predictive accuracy and most reliable uncertainty quantification in both Gaussian and non-Gaussian settings, while Vecchia methods alone offer an attractive alternative when training cost is paramount. GPU acceleration further reduces computation time, enabling scaling to millions of observations.

The case study highlights several scientifically relevant findings. Temperature fields exhibit long-range spatial coherence and persistent anomalies, whereas precipitation shows shorter temporal memory and weaker space-time coupling. Despite these differences, the scalable GP approaches generalize well to unobserved locations, an essential property for forecasting systems with nonuniform station coverage. The methods and software developed here also extend naturally to other large-scale, uncertainty-aware prediction tasks, including ecology, environmental monitoring, and transportation networks.

An important direction for future work is the development of nonstationary or covariate-dependent space-time covariance structures that better capture regional variability in dependence strength and persistence. Correlation-based Vecchia neighbor selection is likely to remain valuable in this setting, as it adapts to local dependence and may help stabilize inference when dependence varies across the domain. The estimation of the covariance smoothness parameter ν could further enhance flexibility and allow the data to inform spatial and temporal regularity. Additional extensions include alternative temporal resolutions (e.g., intraday or weekly) and machine-learning-based mean models combined with spatio-temporal correlation [Sigrist, 2022, 2023, Saha et al., 2023, Zhan and Datta, 2025].

Acknowledgments

This research was partially supported by the Swiss Innovation Agency Innosuisse (grant no. 57667.1 IP-ICT).

References

S. Abdulah, H. Ltaief, Y. Sun, M. G. Genton, and D. E. Keyes. Exageostat: A high performance unified software for geostatistics on manycore systems. *IEEE Transactions on Parallel and Distributed Systems*, 29(12):2771–2784, 2018.

S. Abdullah, F. Alamri, P. Nag, Y. Sun, H. Ltaief, D. E. Keyes, and M. G. Genton. The second competition on spatial statistics for large datasets. *arXiv preprint arXiv:2211.03119*, 2022.

D. Arthur and S. Vassilvitskii. K-means++ the advantages of careful seeding. In *Proceedings of the eighteenth annual ACM-SIAM symposium on Discrete algorithms*, pages 1027–1035, 2007.

S. Banerjee, A. E. Gelfand, A. O. Finley, and H. Sang. Gaussian predictive process models for large spatial data sets. *Journal of the Royal Statistical Society Series B: Statistical Methodology*, 70(4):825–848, 2008.

P. Bauer, A. Thorpe, and G. Brunet. The quiet revolution of numerical weather prediction. *Nature*, 525(7567):47–55, 2015.

H. E. Beck, N. E. Zimmermann, T. R. McVicar, N. Vergopolan, A. Berg, and E. F. Wood. Present and future Köppen-Geiger climate classification maps at 1-km resolution. *Scientific data*, 5(1):1–12, 2018.

T. L. Bell. A space-time stochastic model of rainfall for satellite remote-sensing studies. *Journal of Geophysical Research: Atmospheres*, 92(D8):9631–9643, 1987.

A. Beygelzimer, S. Kakade, and J. Langford. Cover trees for nearest neighbor. In *Proceedings of the 23rd international conference on Machine learning*, pages 97–104, 2006.

C. Bryant, N. R. Wheeler, F. Rubel, and R. H. French. *kgc: Köppen-Geiger climatic zones*, 2017.

S. Chamberlain, D. Hocking, and B. Anderson. Package ‘rnoaa’. 2023.

W. Chen, M. G. Genton, and Y. Sun. Space-time covariance structures and models. *Annual Review of Statistics and Its Application*, 8(1):191–215, 2021.

R. Coe and R. Stern. Fitting models to daily rainfall data. *Journal of Applied Meteorology (1962-1982)*, pages 1024–1031, 1982.

N. Cressie and C. K. Wikle. *Statistics for spatio-temporal data*. John Wiley & Sons, 2011.

A. Datta, S. Banerjee, A. O. Finley, and A. E. Gelfand. Hierarchical nearest-neighbor Gaussian process models for large geostatistical datasets. *Journal of the American Statistical Association*, 111(514):800–812, 2016a.

A. Datta, S. Banerjee, A. O. Finley, N. A. Hamm, and M. Schaap. Nonseparable dynamic nearest neighbor Gaussian process models for large spatio-temporal data with an application to particulate matter analysis. *The Annals of Applied Statistics*, 10(3):1286, 2016b.

A. O. Finley, H. Sang, S. Banerjee, and A. E. Gelfand. Improving the performance of predictive process modeling for large datasets. *Computational statistics & data analysis*, 53(8):2873–2884, 2009.

R. Furrer, M. G. Genton, and D. Nychka. Covariance tapering for interpolation of large spatial datasets. *Journal of Computational and Graphical Statistics*, 15(3):502–523, 2006.

T. Gneiting. Nonseparable, stationary covariance functions for space–time data. *Journal of the American Statistical Association*, 97(458):590–600, 2002.

T. Gneiting, M. G. Genton, and P. Guttorp. Geostatistical space-time models, stationarity, separability, and full symmetry. *Monographs On Statistics and Applied Probability*, 107:151, 2006.

J. Guinness. Permutation and grouping methods for sharpening Gaussian process approximations. *Technometrics*, 60(4):415–429, 2018.

J. Guinness. Gaussian process learning via Fisher scoring of Vecchia’s approximation. *Statistics and Computing*, 31(3):1–8, 2021.

T. Gyger, R. Furrer, and F. Sigrist. Iterative methods for full-scale Gaussian process approximations for large spatial data. *SIAM/ASA Journal on Uncertainty Quantification (in press)*, 2025a.

T. Gyger, R. Furrer, and F. Sigrist. Vecchia-inducing-points full-scale approximations for Gaussian processes. *arXiv preprint arXiv:2507.05064*, 2025b.

M. J. Heaton, A. Datta, A. O. Finley, R. Furrer, J. Guinness, R. Guhaniyogi, F. Gerber, R. B. Gramacy, D. Hammerling, M. Katzfuss, et al. A case study competition among methods for analyzing large spatial data. *Journal of Agricultural, Biological and Environmental Statistics*, 24:398–425, 2019.

Y. M. Idir, O. Orfila, P. Chatellier, and V. Judalet. Improving spatio-temporal Gaussian process modeling with Vecchia approximation: A low-cost sensor-driven approach to urban environmental monitoring. *arXiv preprint arXiv:2511.22500*, 2025.

M. Kang and M. Katzfuss. Correlation-based sparse inverse Cholesky factorization for fast Gaussian-process inference. *Statistics and Computing*, 33(3):56, 2023.

M. Katzfuss. A multi-resolution approximation for massive spatial datasets. *Journal of the American Statistical Association*, 112(517):201–214, 2017.

M. Katzfuss and J. Guinness. A general framework for Vecchia approximations of Gaussian processes. *Statistica Sinica*, 36(1):124–141, 2021.

W. Köppen, E. Volken, and S. Brönnimann. The thermal zones of the earth according to the duration of hot, moderate and cold periods and to the impact of heat on the organic world. *Meteorologische Zeitschrift*, 20(3):351, 2011.

P. Kündig and F. Sigrist. Iterative methods for Vecchia-Laplace approximations for latent Gaussian process models. *Journal of the American Statistical Association*, 120(550):1267–1280, 2025.

F. Lindgren, H. Rue, and J. Lindström. An explicit link between gaussian fields and gaussian markov random fields: the stochastic partial differential equation approach. *Journal of the Royal Statistical Society: Series B (Statistical Methodology)*, 73(4):423–498, 2011.

M. J. Menne, I. Durre, R. S. Vose, B. E. Gleason, and T. G. Houston. An overview of the global historical climatology network-daily database. *Journal of Atmospheric and Oceanic Technology*, 29(7):897–910, 2012.

E. Porcu, R. Furrer, and D. Nychka. 30 years of space–time covariance functions. *Wiley Interdisciplinary Reviews: Computational Statistics*, 13(2):e1512, 2021.

J. Quinonero-Candela and C. E. Rasmussen. A unifying view of sparse approximate Gaussian process regression. *The Journal of Machine Learning Research*, 6:1939–1959, 2005.

F. Rambelli and F. Sigrist. An accuracy-runtime trade-off comparison of scalable Gaussian process approximations for spatial data. *arXiv preprint arXiv:2501.11448*, 2025.

H. Robbins. The empirical bayes approach to statistical decision problems. *The Annals of Mathematical Statistics*, 35(1):1–20, 1964.

A. Saha, S. Basu, and A. Datta. Random forests for spatially dependent data. *Journal of the American Statistical Association*, 118(541):665–683, 2023.

H. Sang and J. Z. Huang. A full scale approximation of covariance functions for large spatial data sets. *Journal of the Royal Statistical Society Series B: Statistical Methodology*, 74(1):111–132, 2012.

B. Sansó and L. Guenni. A bayesian approach to compare observed rainfall data to deterministic simulations. *Environmetrics: The official journal of the International Environmetrics Society*, 15(6):597–612, 2004.

F. Sigrist. Gaussian process boosting. *Journal of Machine Learning Research*, 23(232):1–46, 2022.

F. Sigrist. Latent Gaussian model boosting. *IEEE Transactions on Pattern Analysis and Machine Intelligence*, 45(2):1894–1905, 2023.

F. Sigrist, H. R. Künsch, and W. A. Stahel. A dynamic nonstationary spatio-temporal model for short term prediction of precipitation. *The Annals of Applied Statistics*, pages 1452–1477, 2012.

C. Stidd. Estimating the precipitation climate. *Water Resources Research*, 9(5):1235–1241, 1973.

A. Terenin, D. R. Burt, A. Artemev, S. Flaxman, M. van der Wilk, C. E. Rasmussen, and H. Ge. Numerically stable sparse Gaussian processes via minimum separation using cover trees. *arXiv preprint arXiv:2210.07893*, 2022.

L. Tierney and J. B. Kadane. Accurate approximations for posterior moments and marginal densities. *Journal of the American Statistical Association*, 81(393):82–86, 1986.

J. Tobin. Estimation of relationships for limited dependent variables. *Econometrica: journal of the Econometric Society*, pages 24–36, 1958.

C. Varin, N. Reid, and D. Firth. An overview of composite likelihood methods. *Statistica Sinica*, pages 5–42, 2011.

A. V. Vecchia. Estimation and model identification for continuous spatial processes. *Journal of the Royal Statistical Society Series B: Statistical Methodology*, 50(2):297–312, 1988.

D. S. Wilks. Multisite downscaling of daily precipitation with a stochastic weather generator. *Climate Research*, 11:125–136, 1999.

C. K. Williams and C. E. Rasmussen. *Gaussian processes for machine learning*. MIT Press Cambridge, MA, 2006.

W. Zhan and A. Datta. Neural networks for geospatial data. *Journal of the American Statistical Association*, 120(549):535–547, 2025.

Appendices

A Dataset

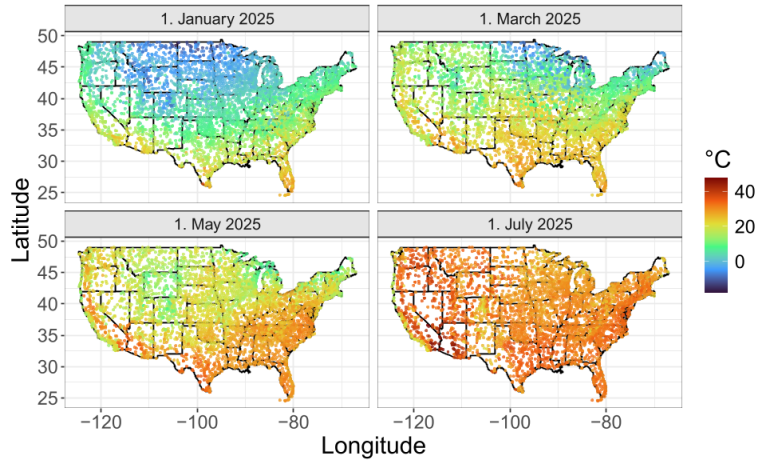


Figure 5: Daily maximum temperature ($^{\circ}\text{C}$ with resolution: 0.1) across the conterminous United States, shown for four selected dates in 2025.

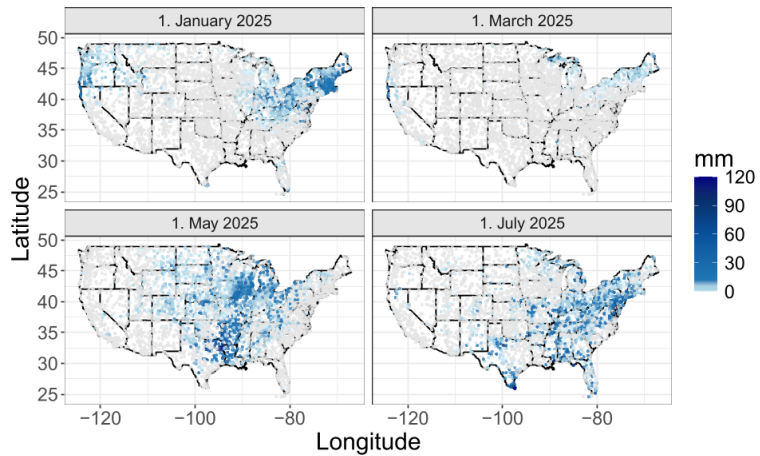


Figure 6: Daily rainfall in millimeters (mm) across the conterminous United States at four selected days in 2025.

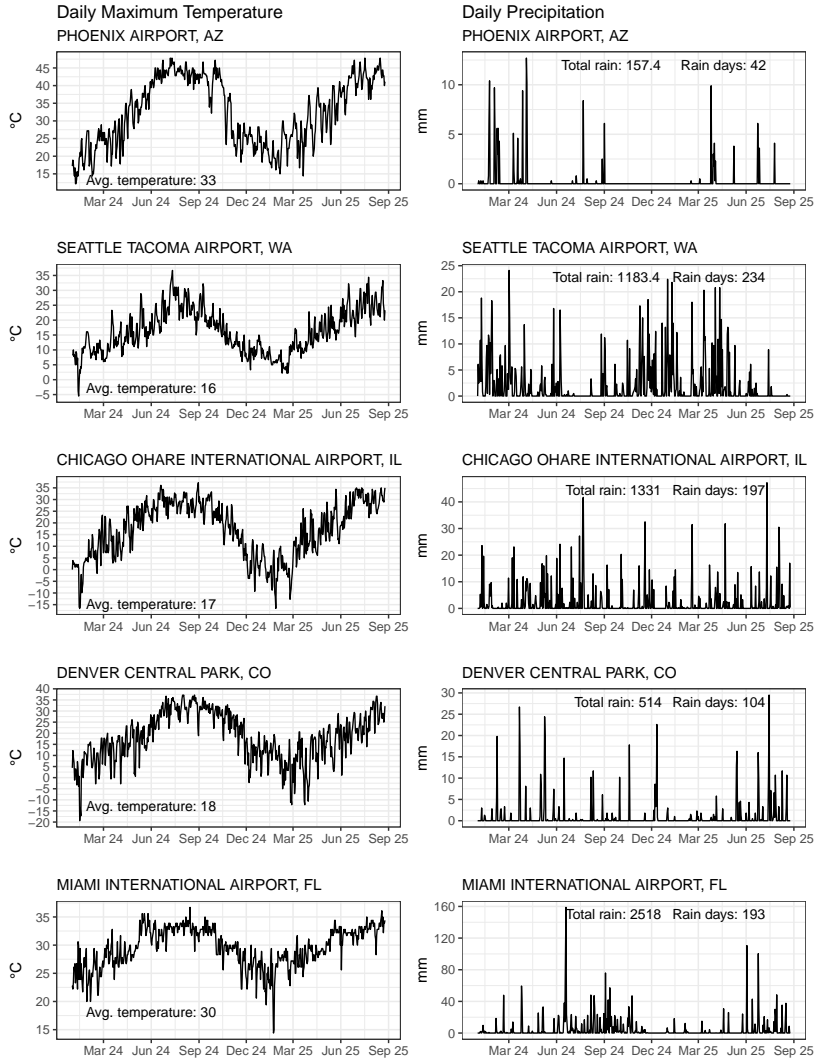


Figure 7: Daily maximum temperature ($^{\circ}\text{C}$) and precipitation (mm) at five representative GHCN stations across the full study period, with annotated average temperature, total rain amount (mm), and counts of rainy days (precipitation > 0 mm). Note the different scales in the panels.

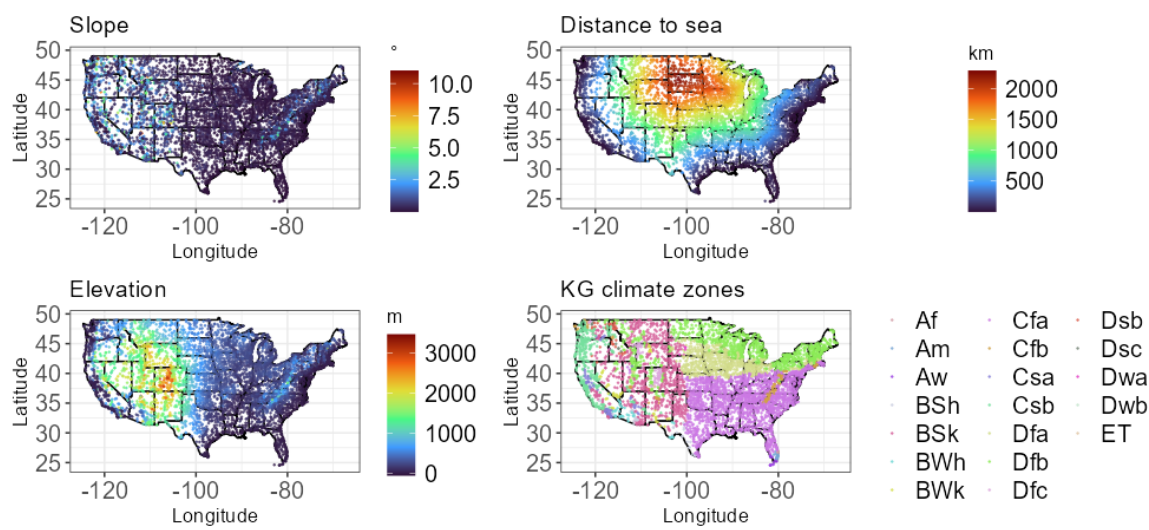


Figure 8: Example geographic and climatic covariates used in the model.

B Selecting Vecchia neighbors and inducing points

Algorithm 2 Construction of cover tree for correlation-based Vecchia neighbor search

Input: Set of data points $\mathcal{D} = \{(\mathbf{s}_1, t_1), \dots, (\mathbf{s}_n, t_n)\}$
Output: Cover tree \mathcal{CT}

- 1: Initialize: Maximal distance: $R_{\max} = 1$
 Empty tree: \mathcal{CT}
 Knot set of \mathcal{CT} : $\mathcal{V} \leftarrow \{\}$
 Number of levels in \mathcal{CT} : $l \leftarrow 0$
 Covered data points per level and knot: $\mathcal{C}_{0,0} \leftarrow \mathcal{S}$
- 2: Set root in \mathcal{CT} : $\mathcal{CT}_{1,1} \leftarrow (\mathbf{s}_1, t_1)$, $\mathcal{V} \leftarrow \{(\mathbf{s}_1, t_1)\}$, $l \leftarrow 1$, $\mathcal{C}_{l,(\mathbf{s}_1, t_1)} \leftarrow \mathcal{C}_{0,0} \setminus \{(\mathbf{s}_1, t_1)\}$
- 3: **while** $\text{size}(\mathcal{V}) < n$ **do**
- 4: $R_l \leftarrow R_{\max}/2^l$ ▷ New maximal distance between new knots in tree \mathcal{CT} and descendants
- 5: $\mathcal{K} \leftarrow \mathcal{CT}_{l,:}$ ▷ Set of knots of tree \mathcal{CT} in level l
- 6: **for** $k \in \mathcal{K}$ **do**
- 7: $\text{ind} \leftarrow 0$ ▷ Index of knot in tree \mathcal{CT} at level $l+1$
- 8: **while** $\mathcal{C}_{l,k} \neq \{\}$ **do**
- 9: $\text{ind} \leftarrow \text{ind} + 1$
- 10: $\mathcal{CT}_{l+1,\text{ind}} \leftarrow \{(\mathbf{s}_i, t_i) \in \mathcal{C}_{l,k} \mid i = \min\{j \mid (\mathbf{s}_j, t_j) \in \mathcal{C}_{l,k}\}$ ▷ Point with smallest index in $\mathcal{C}_{l,k}$
- 11: $\mathcal{V} \leftarrow \mathcal{V} \cup \{\mathcal{CT}_{l+1,\text{ind}}\}$
- 12: $\mathcal{C}_{l,k} \leftarrow \mathcal{C}_{l,k} \setminus \{\mathcal{CT}_{l+1,\text{ind}}\}$
- 13: $\mathcal{C}_{l+1,\mathcal{CT}_{l+1,\text{ind}}} \leftarrow \{(\mathbf{s}_i, t_i) \in \mathcal{C}_{l,k} \mid d_c((\mathbf{s}_i, t_i), \mathcal{CT}_{l+1,\text{ind}}) \leq R_l\}$
- 14: $\mathcal{C}_{l,k} \leftarrow \mathcal{C}_{l,k} \setminus \mathcal{C}_{l+1,\mathcal{CT}_{l+1,\text{ind}}}$
- 15: **end while**
- 16: **end for**
- 17: $l \leftarrow l + 1$
- 18: **end while**

Algorithm 3 Find m_v nearest Vecchia neighbors with respect to the metric d_c

Input: Query point $(\mathbf{s}_i, t_i) \in \mathcal{D}$, cover tree \mathcal{CT} , number of neighbors m_v
Output: \mathcal{N}_{m_v} , set of m_v nearest Vecchia neighbors of (\mathbf{s}_i, t_i)

- 1: Initialize: Maximal distance: $R_{\max} = 1$
 Number of levels in tree \mathcal{CT} : $l \leftarrow \text{depth}(\mathcal{CT})$
 Set of potential nearest neighbors: $\mathcal{Q} \leftarrow \{\mathcal{CT}_{1,1}\}$
 Distance to m_v closest point in \mathcal{Q} : $D_{m_v} \leftarrow 1$ ▷ Set to 1 if $|\mathcal{Q}| < m_v$
- 2: **for** $j = 1$ to l **do**
- 3: $\mathcal{C} \leftarrow \{(\mathbf{s}_k, t_k) \in \text{Children}((\mathbf{s}, t)) \mid (\mathbf{s}, t) \in \mathcal{Q} \cap k < i\} \cup \mathcal{Q}$ ▷ Children of \mathcal{Q} with index $< i$
- 4: $D_{m_v} \leftarrow m_v\text{-th smallest distance } d_c((\mathbf{s}, t), (\mathbf{s}_i, t_i)) \text{ for } (\mathbf{s}, t) \in \mathcal{C}$ ▷ Set to 1 if $|\mathcal{C}| < m_v$
- 5: $\mathcal{Q} \leftarrow \{(\mathbf{s}, t) \in \mathcal{C} \mid d_c((\mathbf{s}, t), (\mathbf{s}_i, t_i)) \leq D_{m_v} + 1/2^{j-1}\}$
- 6: **end for**
- 7: $\mathcal{N}_{m_v} \leftarrow \text{Find } m_v \text{ nearest points to } (\mathbf{s}_i, t_i) \text{ in } \mathcal{Q} \text{ by brute-force search}$

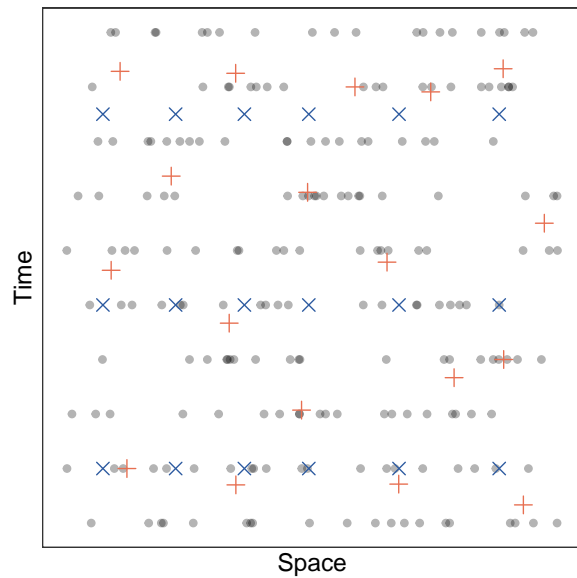


Figure 9: The joint ($+$; eighteen unique space-time points) and space-time separated (\times ; three unique time points and six unique space points) inducing point selection. Black points indicate the space-time locations of the observed data.

C Simulation study: Additional plots

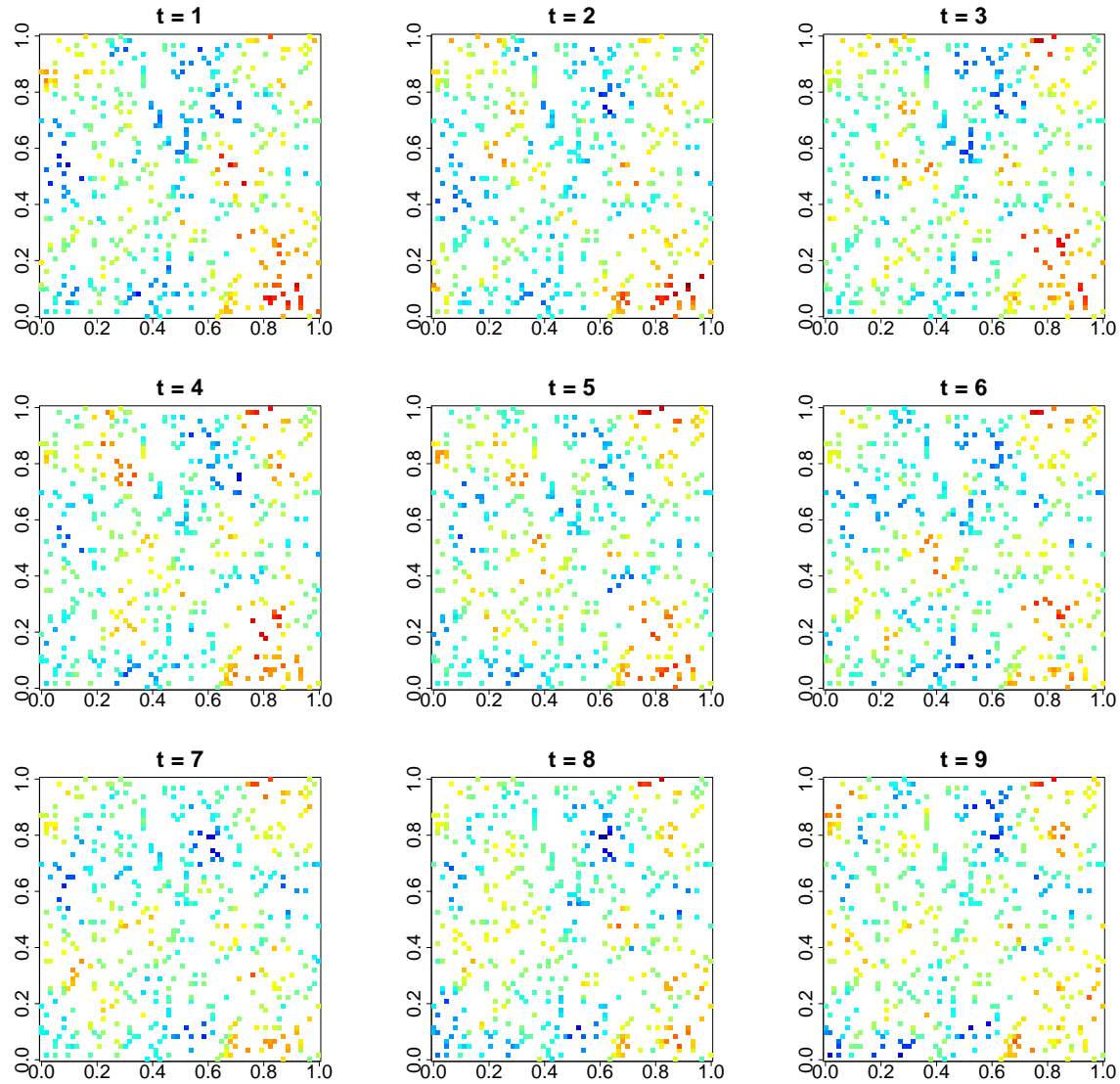


Figure 10: Synthetic space-time dataset for first nine time points $t \in \{1, 2, 3, 4, 5, 6, 7, 8, 9\}$ with 500 spatial locations per time point.

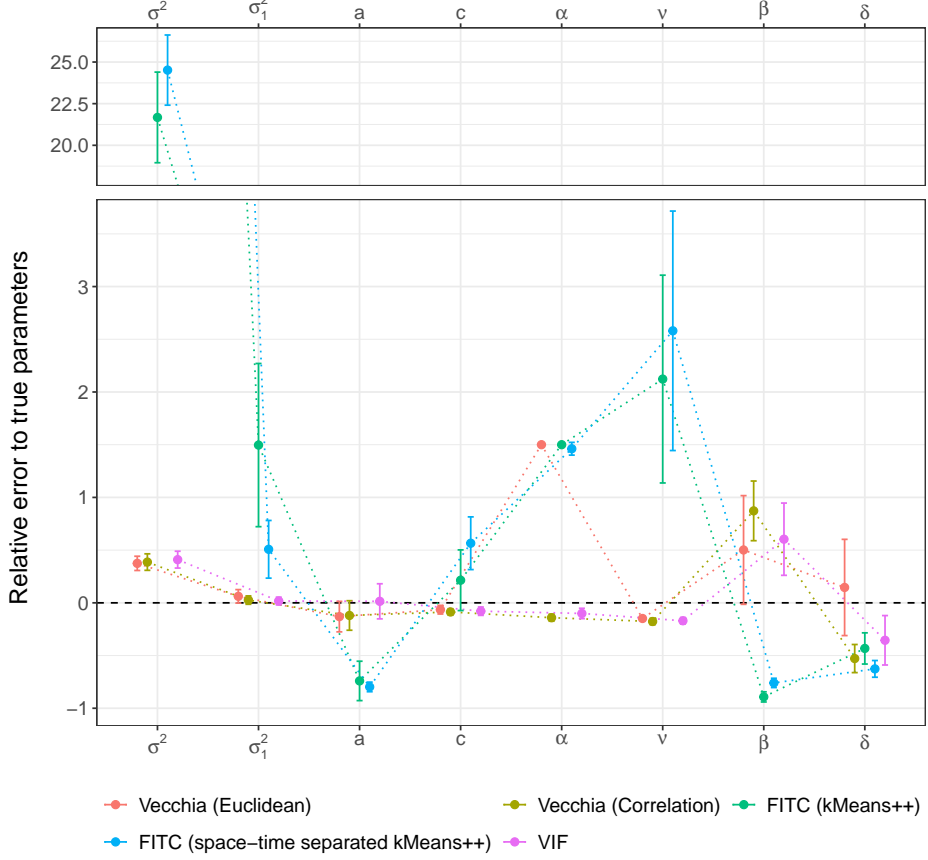


Figure 11: Relative error with error bars (mean \pm two standard errors) of covariance parameters for Vecchia, FITC, and VIF approximations.

D Space-time model benchmark: Additional plots and tables

Data set	σ_1^2	a	c	α	ν	β	δ	Time range	effective	Space range	effective
\mathcal{D}_1	0.9	1	50	0.6	1	0.9	0.1	11.63		0.08	
\mathcal{D}_2	0.9	0.24	12.5	0.6	1	0.9	0.1	38.20		0.32	
\mathcal{D}_3	0.9	1	2.5	0.08	1	0.9	0.1	∞		1.6	

Table 4: The parameter choices for the experiments in the sub-competition 2a and 2b in [Abdulah et al., 2022].

The `Envstat.ai` team employed a Deep Neural Network (DNN) for spatio-temporal prediction, extending the spatial model of Chen et al. [2020]. They incorporated basis functions to capture spatio-temporal dependence. For interpolation tasks, they applied regression, while for forecasting at new locations they adopted a two-stage strategy: (i) interpolate values at the new locations for observed time points, and (ii) train a Long Short-Term Memory (LSTM) network on these interpolated values to obtain forecasts for future time points.

The `GpGp` team fitted a Matérn space-time covariance function using the `GpGp` package to estimate the model parameters. The two estimated range parameters were then used to rescale the coordinates, which guided the ordering and neighbor selection for Vecchia's approximation. They employed $m_v = 30$ neighbors to fit the model and $m_v = 60$ for prediction.

The `RESSTE` team began with an exploratory data analysis using a space-time covariance function

and identified that the data were generated from a positively non-separable space-time kernel. Based on this finding, they selected a covariance function from the Gneiting class, combining a Matérn spatial covariance with a Cauchy temporal covariance. Given the large size of the datasets, they used a block-composite likelihood to separately estimate the spatial and temporal parameters, which were then combined to fit the full space-time model. For prediction, they applied ordinary kriging, conditioning on a specified number of nearest spatial neighbors as well as preceding, current, and subsequent time slots.

The **GeoModels** team applied the nearest neighbor weighted composite likelihood method to model both datasets, using the **GeoModels** package [Bevilacqua et al., 2022].

Table 5 presents the RMSE of the VIF approximation across all datasets and prediction scenarios from sub-competition *2b* compared to the four best competitors: **Envstat.ai**, **GpGp**, **GeoModels**, **RESSTE** described above. Overall, the VIF approximation performs strongly across all datasets and scenarios. For the time-extrapolation scenario T10, **Envstat.ai** is clearly superior to all competing methods.

RMSE		VIF	<i>Envstat.ai</i>	<i>GpGp</i>	<i>GeoModels</i>	<i>RESSTE</i>
RS	\mathcal{D}_1	0.276685	0.536665	0.277007	0.276670	0.276730
	\mathcal{D}_2	0.071518	0.232439	0.071519	0.071517	0.071523
	\mathcal{D}_3	0.014095	0.050975	0.014096	0.014098	0.014097
RST	\mathcal{D}_1	0.257556	0.538314	0.274177	0.276957	0.264053
	\mathcal{D}_2	0.070873	0.232796	0.070873	0.070880	0.071254
	\mathcal{D}_3	0.014260	0.050681	0.014260	0.014269	0.013380
T10	\mathcal{D}_1	0.890374	0.522757	0.904975	0.888390	0.903714
	\mathcal{D}_2	0.947473	0.206519	0.949491	0.948918	0.964134
	\mathcal{D}_3	0.677872	0.047245	0.651425	0.728364	0.688624
Time		69,063 s	-	-	-	-

Table 5: RMSE for the sub-competition *2b* of Abdulah et al. [2022].

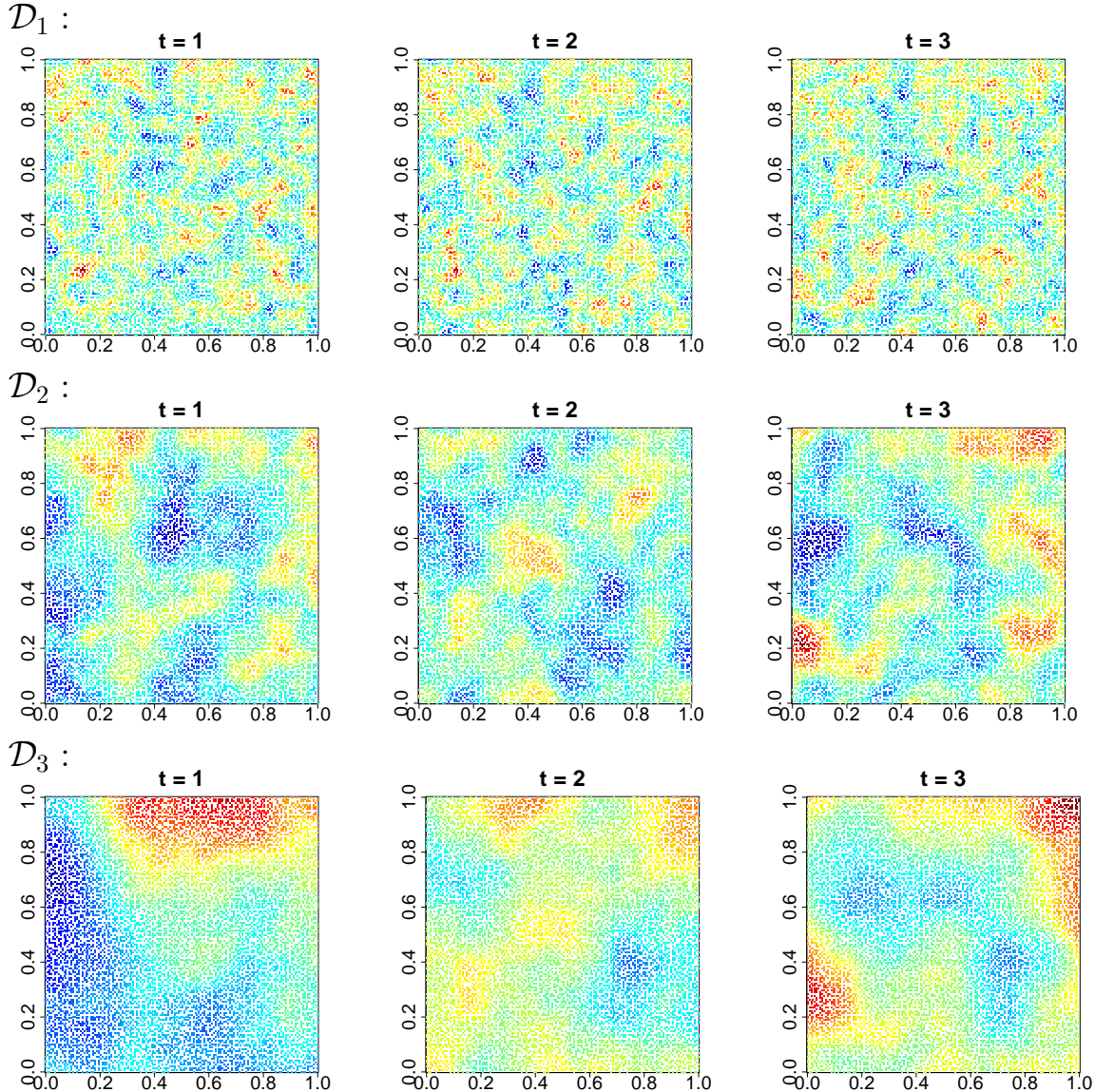


Figure 12: Synthetic space-time datasets \mathcal{D}_1 (top), \mathcal{D}_2 (middle), and \mathcal{D}_3 (bottom) for first three time points $t \in \{1, 2, 3\}$ with 10,000 spatial locations per time point.

E GPU acceleration: Additional plots and tables

Time	Vecchia Euclidean	Vecchia Correlation	FITC kMeans++	FITC sts-kMeans++	VIF
CPU	1131 s	18873 s	2935 s	2942 s	69063 s
GPU	759 s	1350 s	743 s	756 s	5847 s
Speedup	1.49	13.98	3.95	3.89	11.81

Table 6: Average end-to-end runtime (training + prediction, in seconds) for sub-competition \mathcal{B} of Abdulah et al. [2022], comparing CPU and GPU execution and the resulting speedups.

Figure 13 reports runtimes and speedups for a single optimization iteration for GP models with a non-Gaussian likelihoods, comprising two marginal log-likelihood evaluations, gradient computations, and two Vecchia neighbor searches, across sample sizes and approximation strategies.

Figure 14 reports runtimes and speedups for a single optimization iteration for high-dimensional

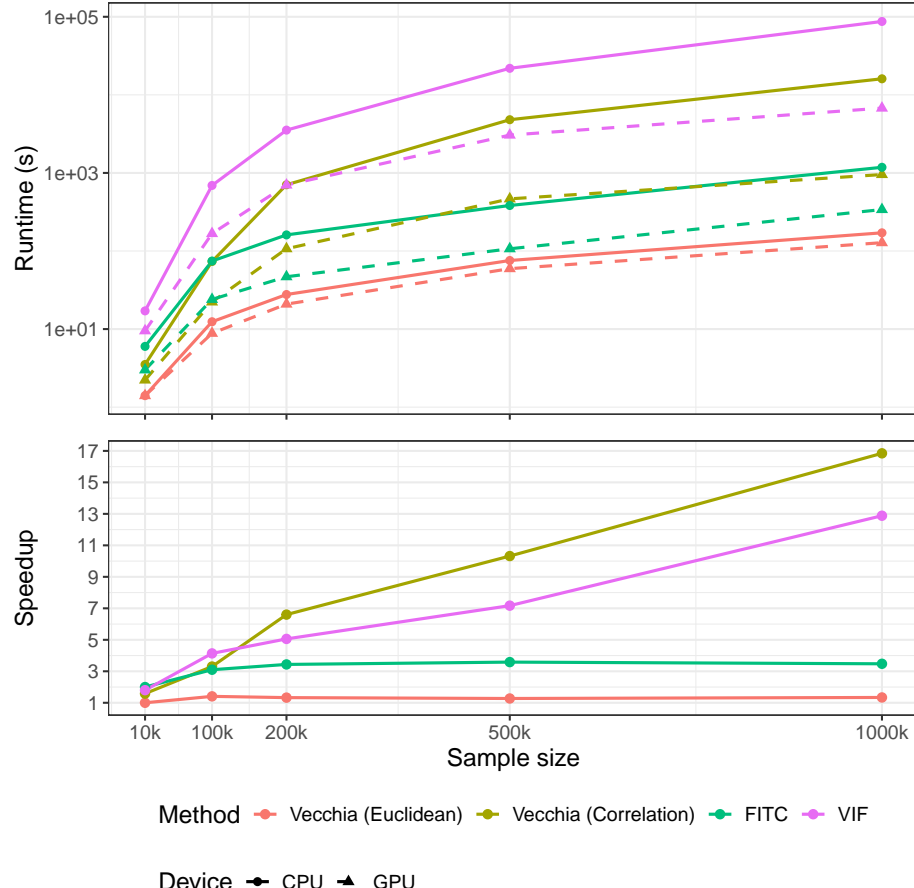


Figure 13: Runtimes in seconds (log-scale) and GPU speedups for a single parameter-optimization iteration of a latent GP model with a non-Gaussian likelihood, consisting of two Laplace-approximated evaluations of the negative log-marginal likelihood, gradient computations for all covariance parameters, and two Vecchia neighbor searches. Results are shown for varying sample sizes and for the Vecchia, FITC, and VIF approximations.

inputs modeled using ARD Matérn kernels, comprising two negative log-likelihood evaluations, gradient computations, and two Vecchia neighbor searches, across various input dimensions and approximation strategies.

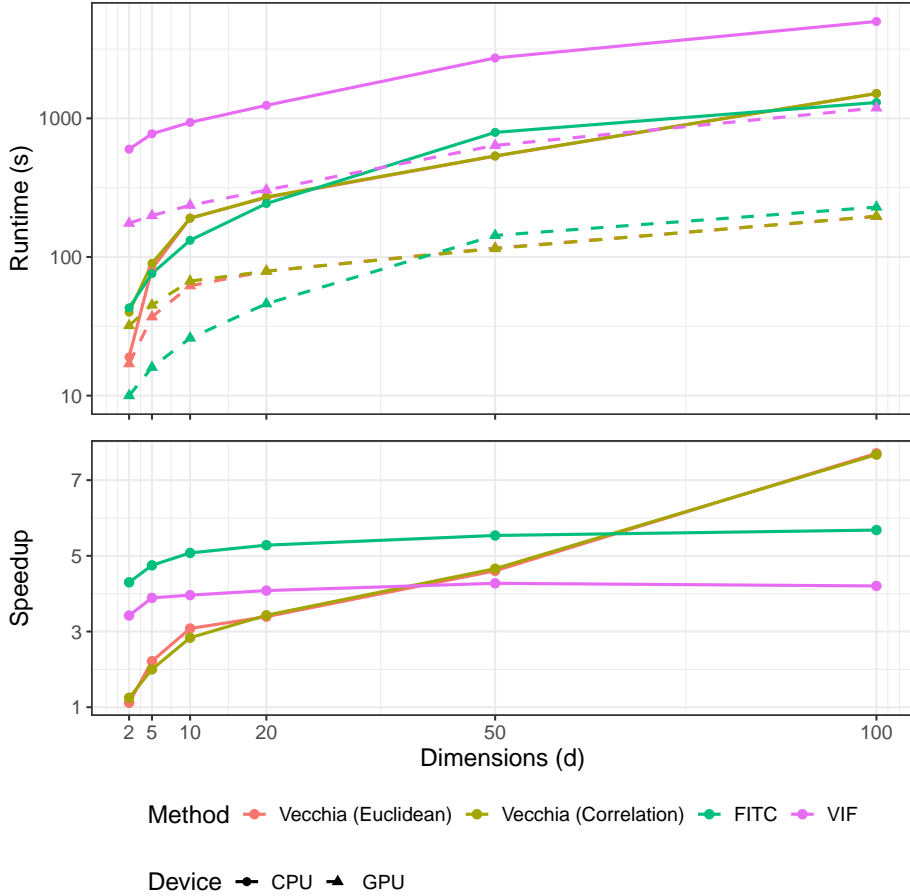


Figure 14: Runtimes in seconds (log-scale) and GPU speedups for a single parameter-optimization iteration of a GP model with d -dimensional inputs and an ARD Matérn covariance function, consisting of two negative log-likelihood evaluations, gradient computations for all covariance parameters, and two Vecchia neighbor searches. Results are shown for varying sample sizes and for the Vecchia, FITC, and VIF approximations with a fixed sample size of 200,000.

F Real-world application: Additional plots and tables

		Vecchia Euclidean	Vecchia Correlation	FITC kMeans++	FITC Space-time kMeans++	VIF
Temporal forecasting	RMSE	2.808	2.749	3.422	3.292	2.737
	CRPS	1.626	1.578	2.046	1.978	1.573
Spatio-temporal forecasting	RMSE	2.829	2.759	3.448	3.311	2.749
	CRPS	1.633	1.581	2.060	1.987	1.577
Runtime		Train Prediction	835 s 33 s	1541 s 46 s	1234 s 20 s	6543 s 113 s

Table 7: Overall five-day RMSE, CRPS, and average computational runtimes. Training time corresponds to parameter estimation; prediction time corresponds to prediction of means and variances.

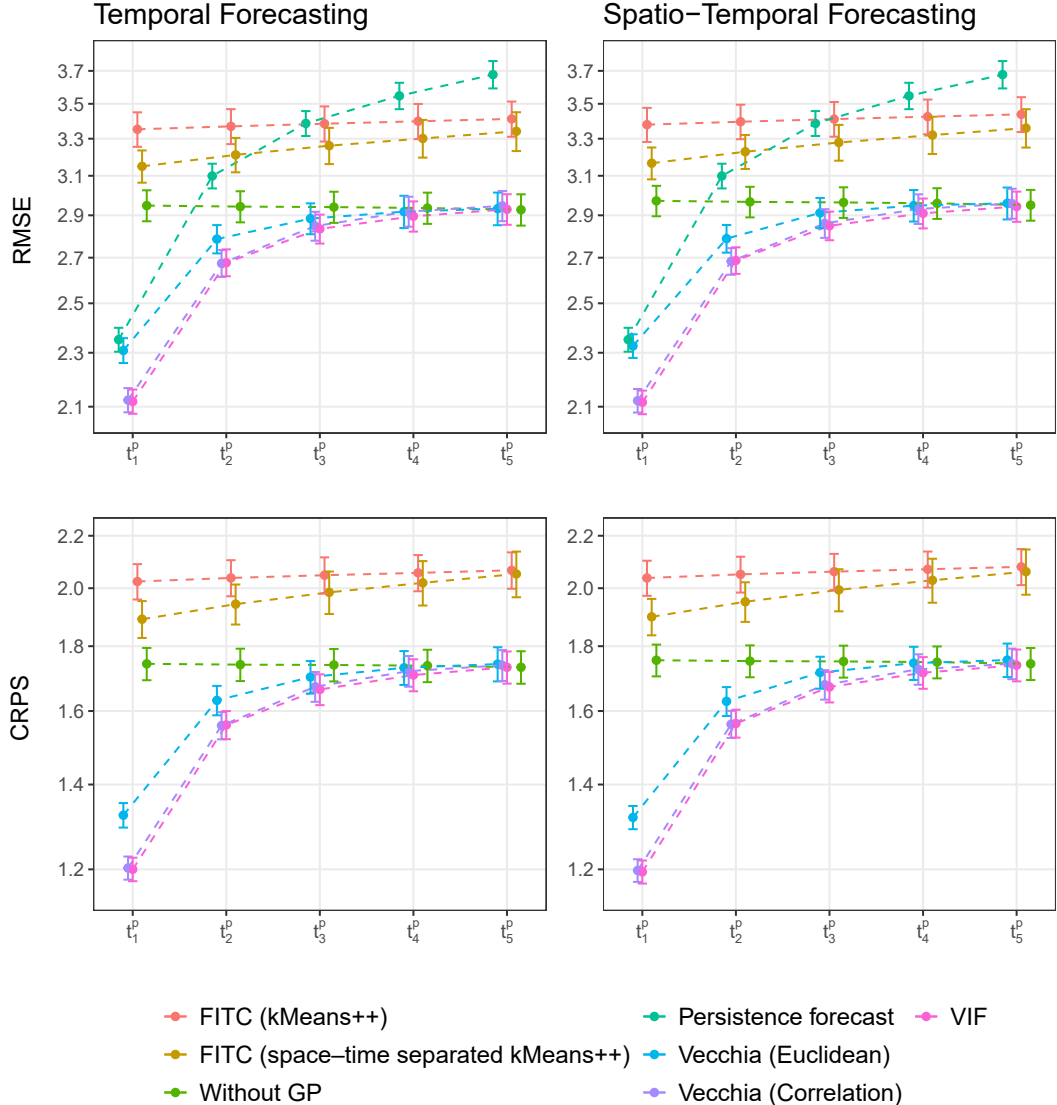


Figure 15: Day-wise RMSE and CRPS (log scale) with error bars (mean \pm one standard error) for one- to five-day temperature forecasts under the temporal, and the spatio-temporal forecasting settings. Methods include the Vecchia approximation with Euclidean- and correlation-based neighbors ($m_v = 30$), FITC with standard and space-time separated kMeans++ inducing points ($m = 500$), and VIF ($m_v = 30$, $m = 500$). A persistence forecast and a fixed-effects-only regression model (without GP) are included for comparison.

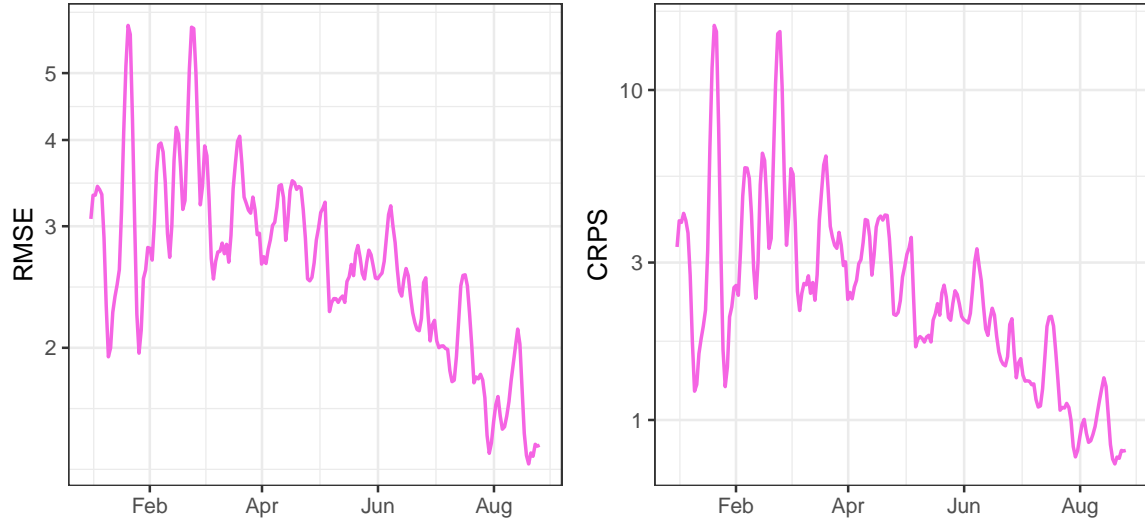


Figure 16: Evolution of overall five-day temperature forecast error (RMSE and CRPS, log scale) for the VIF approximation throughout 2025.

Date	σ^2	σ_1^2	a	c	α	β	δ	Time range	Space range
Dec 24	1.379	5.497	0.087	3.47e-06	0.842	0.998	1.643	6.6 days	1,367 km
Jan 25	1.387	5.635	0.087	3.47e-06	0.840	0.999	1.647	6.7 days	1,367 km
Feb 25	1.414	5.775	0.087	3.48e-06	0.839	0.998	1.650	6.7 days	1,367 km
Mar 25	1.464	6.058	0.088	3.50e-06	0.831	0.999	1.656	6.7 days	1,355 km
Apr 25	1.540	6.307	0.089	3.39e-06	0.823	0.998	1.662	6.8 days	1,399 km
May 25	1.573	6.407	0.090	3.35e-06	0.825	0.997	1.668	6.7 days	1,416 km
Jun 25	1.561	6.366	0.089	3.37e-06	0.826	0.998	1.671	6.7 days	1,408 km
Jul 25	1.539	6.193	0.090	3.37e-06	0.831	0.999	1.667	6.7 days	1,408 km

Table 8: Estimated covariance parameters for the VIF model at each re-estimation, with effective ranges reported as the time or distance at which correlation decays to 0.05.

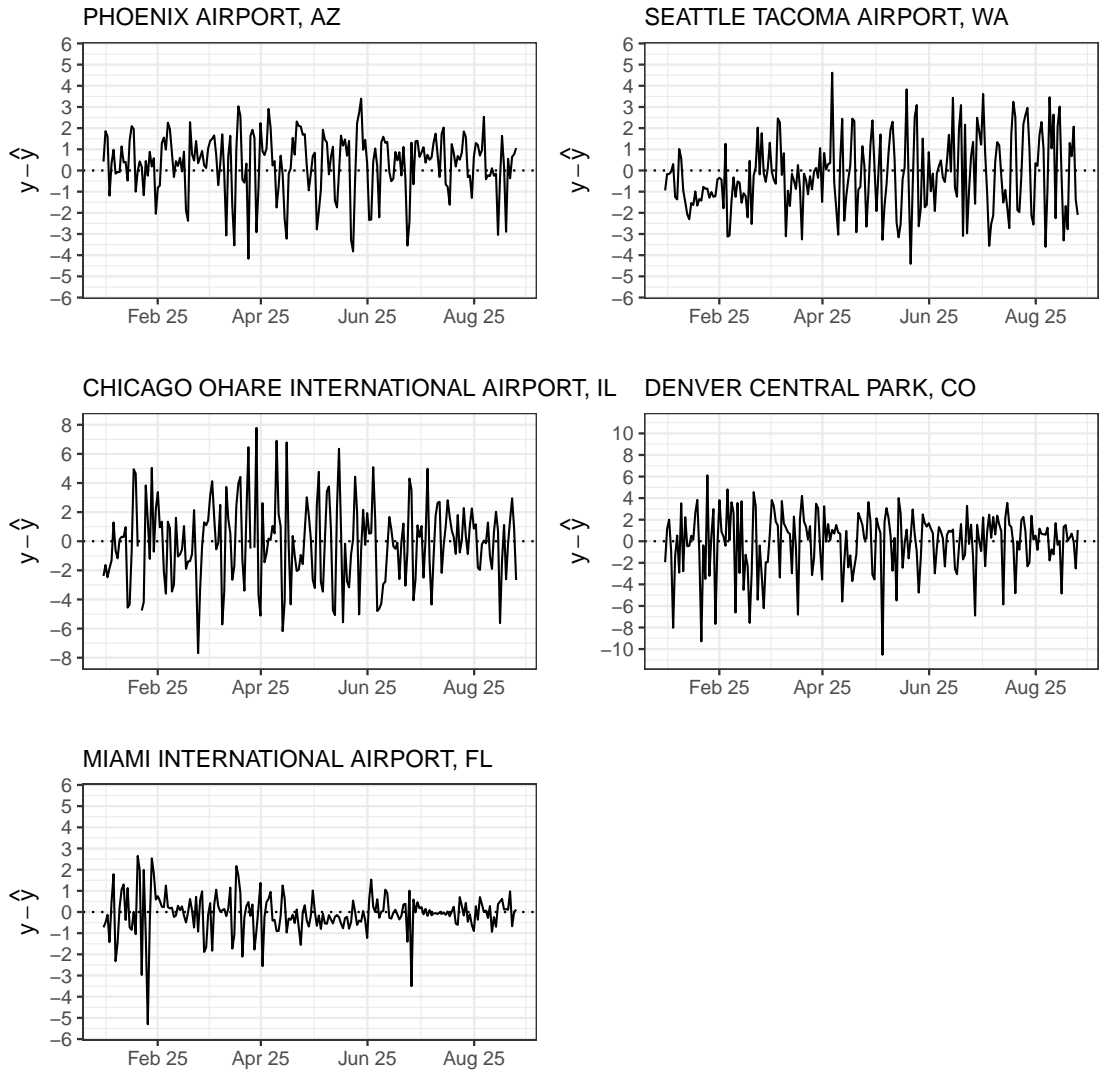


Figure 17: One-day-ahead maximal temperature forecast residuals for five representative GHCN stations across the full prediction period.

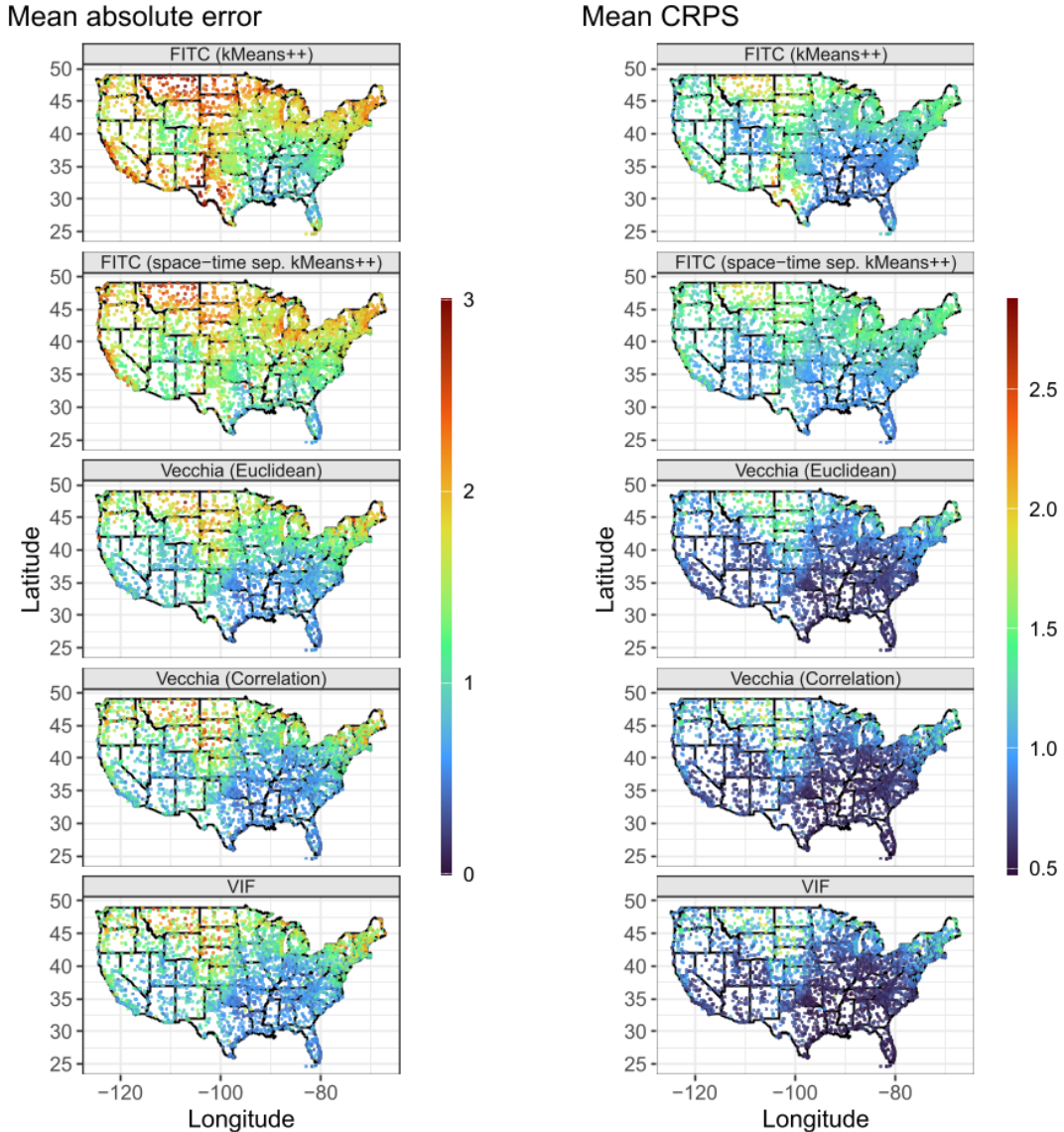


Figure 18: Mean absolute error and mean CRPS of one-day-ahead forecasts for August 2025, computed per station for the Vecchia (Euclidean and correlation-based; $m_v = 30$), FITC (standard and space-time separated kMeans++; $m = 500$), and VIF ($m_v = 30$, $m = 500$) approximations.

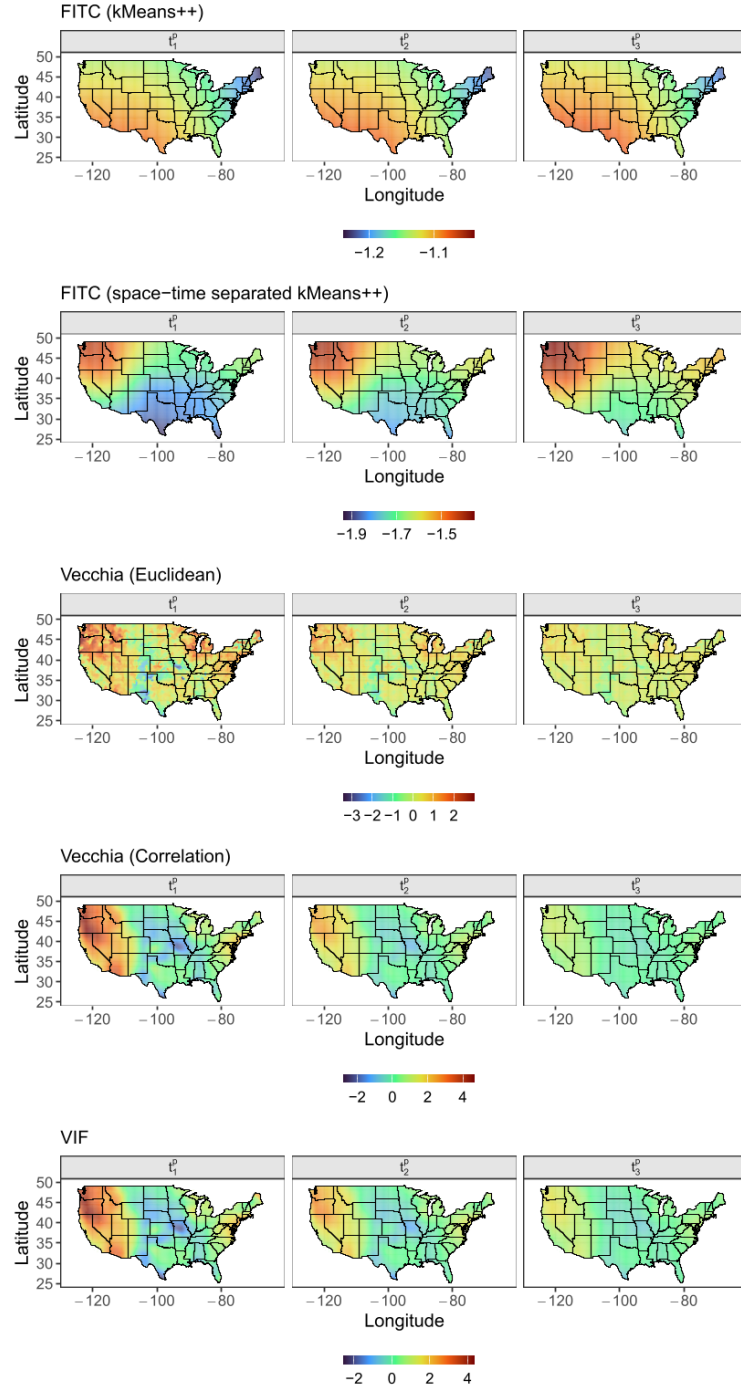


Figure 19: Estimated GP random effects at the final re-estimation step for the temperature data across the conterminous United States for multiple temporal lags, shown for the Vecchia (Euclidean and correlation-based), FITC (standard and space-time separated kMeans++), and VIF approximations.

F.1 PIT reliability diagrams (temperature)

The PIT reliability diagrams in Figure 20 show generally good calibration for the VIF and Vecchia approximations across all lead times, with PIT CDFs closely tracking the diagonal uniform reference. Calibration remains relatively stable from one- to five-day lead times, with only minor dispersion differences across horizons. Differences between the Vecchia (Euclidean and correlation-based) and VIF approaches are small at the aggregate level. In contrast, both FITC variants exhibit noticeably poorer calibration across all lead times, with systematic deviations from the diagonal indicative of bias and misrepresentation of uncertainty. Residual departures from uniformity across all methods point to remaining lead-dependent dispersion errors and mild tail effects.

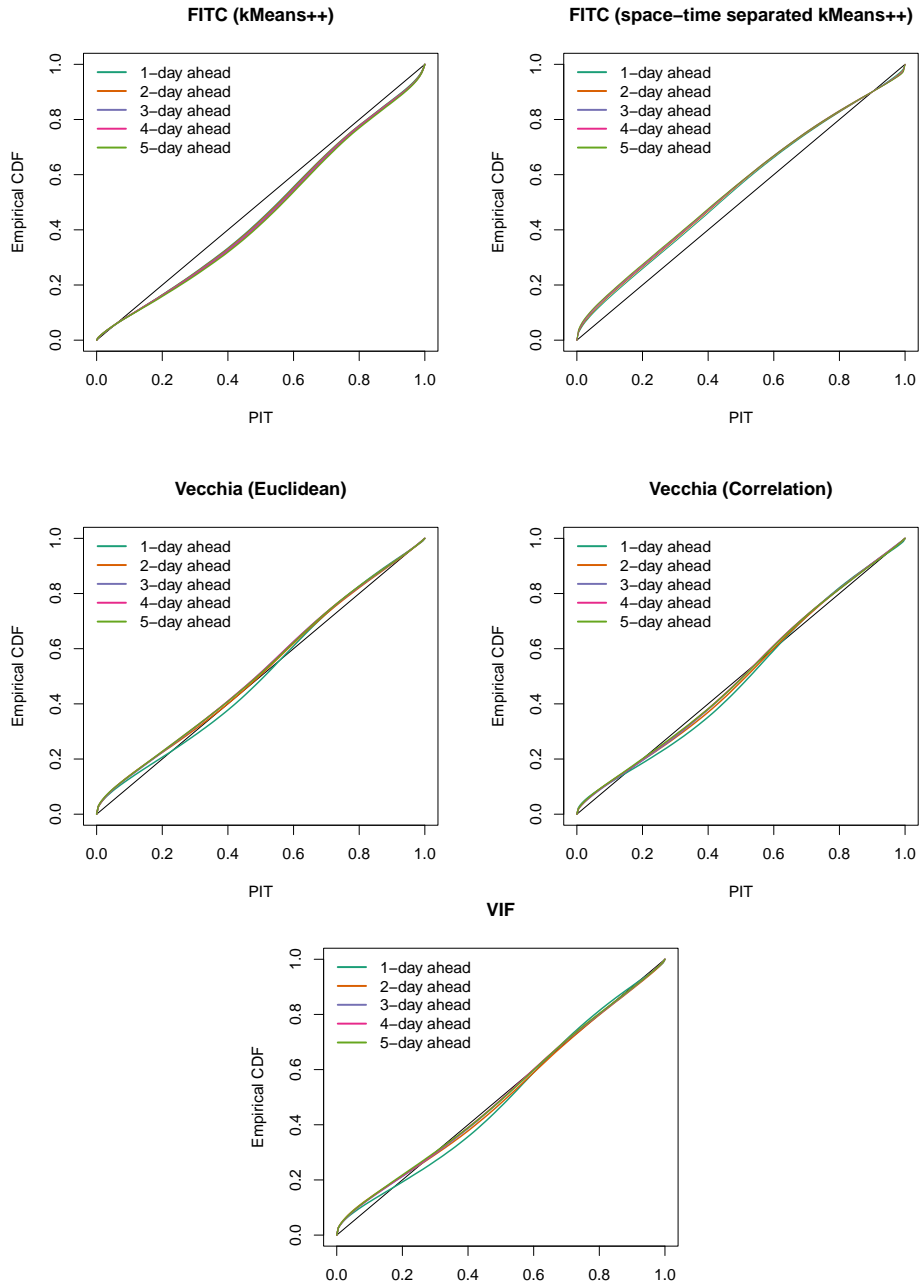


Figure 20: PIT reliability diagrams for temperature forecasts using VIF, FITC, and Vecchia approximations. Curves show $\text{uniform}(0,1)$ QQ-plots for the empirical PIT CDFs for forecast instances pooled over all stations and shown separately for each lead time from one to five days. The black diagonal indicates perfect calibration.

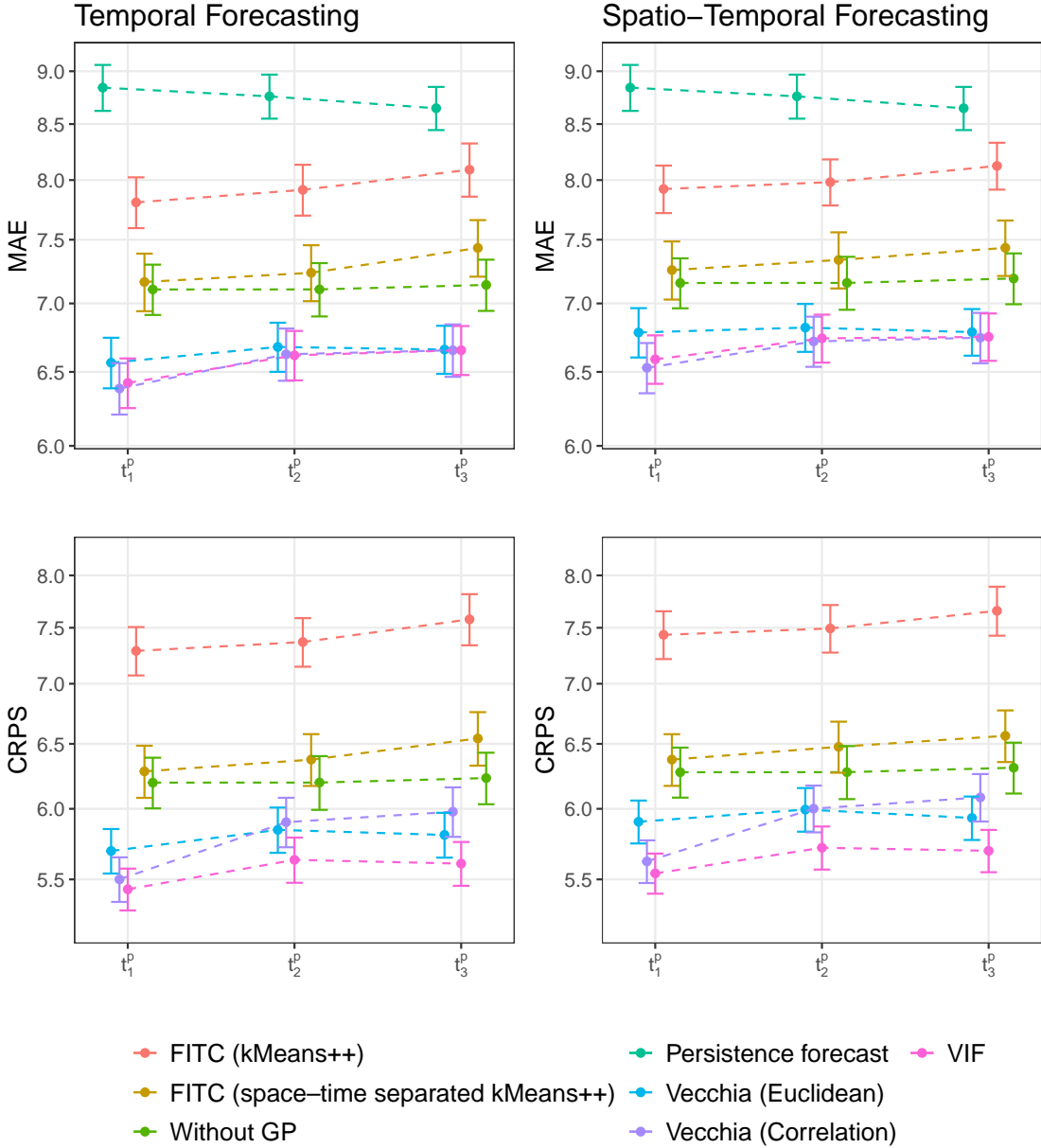


Figure 21: Day-wise MAE and CRPS (log scale) with error bars (mean \pm one standard error) for one-to three-day precipitation amount forecast under the temporal, and the spatio-temporal forecasting settings. Methods include the Vecchia approximation with Euclidean- and correlation-based neighbors ($m_v = 30$), FITC with standard and space-time separated kMeans++ inducing points ($m = 500$), and VIF ($m_v = 30$, $m = 500$). A persistence forecast and a fixed-effects-only regression model (without GP) are included for comparison.

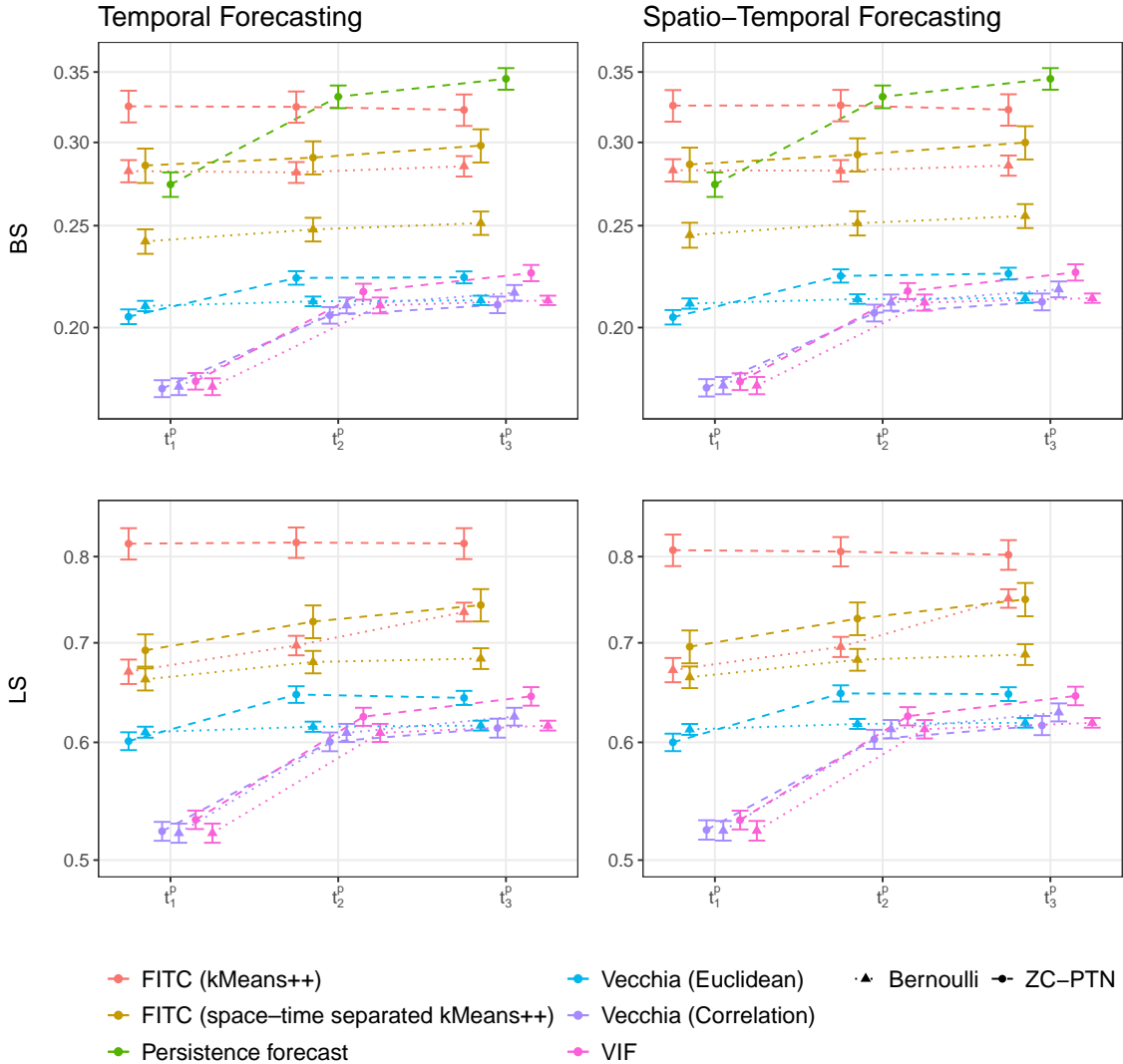


Figure 22: Day-wise BS and LS (log scale) with error bars (mean \pm one standard error) for one- to three-day precipitation occurrence forecast under the temporal, and the spatio-temporal forecasting settings. Methods include the Vecchia approximation with Euclidean- and correlation-based neighbors ($m_v = 30$), FITC with standard and space-time separated kMeans++ inducing points ($m = 500$), and VIF ($m_v = 30$, $m = 500$). A persistence forecast and results for the Bernoulli likelihood are included for comparison.

		Vecchia Euclidean	Vecchia Correlation	FITC kMeans++	FITC Space-time kMeans++	VIF
Temporal forecasting	MAE	6.634	6.551	7.941	7.280	6.571
	CRPS	5.780	5.790	7.412	6.404	5.560
	BS	0.217	0.197	0.324	0.291	0.207
	LS	0.630	0.579	0.806	0.719	0.600
Spatio-temporal forecasting	MAE	6.801	6.664	8.014	7.341	6.694
	CRPS	5.942	5.901	7.533	6.474	5.653
	BS	0.218	0.198	0.324	0.293	0.207
	LS	0.631	0.581	0.817	0.724	0.601
Runtime	Train	3,321 s	5,618 s	2,201 s	2,187 s	10,728 s
	Prediction	201 s	278 s	28 s	29 s	413 s

Table 9: The average overall MAE, CRPS, BS, and LS for the Vecchia approximation with Euclidean- and correlation-based neighbor selection, the FITC approximation with inducing points selected via standard and space-time separated kMeans++, and the VIF approximation. The results distinguish between temporal forecasting, and spatio-temporal forecasting. Average runtimes in seconds (s) are shown for parameter estimation (Train) and computation of predictive mean and variances (Prediction).

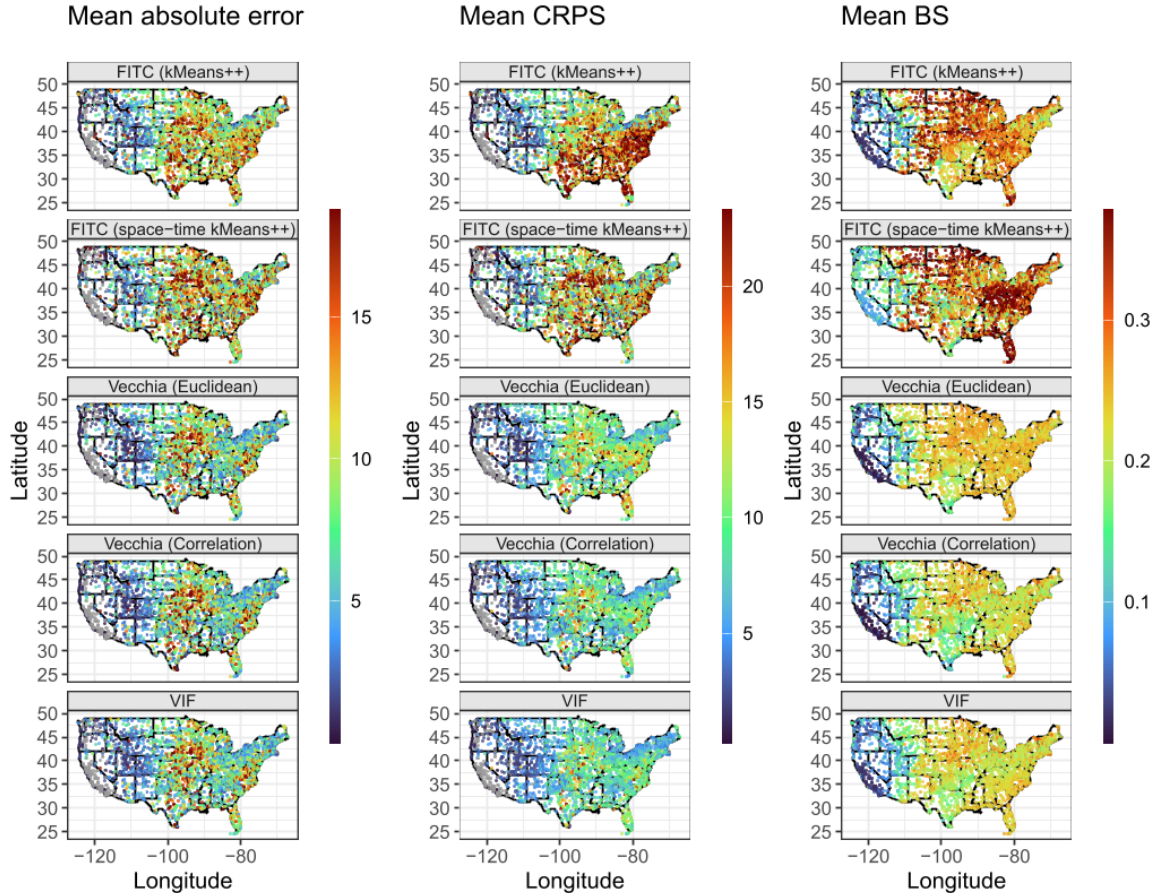


Figure 23: Mean absolute error, mean CRPS, and mean BS of one-day-ahead forecasts for August 2025, computed per station for the Vecchia (Euclidean and correlation-based; $m_v = 30$), FITC (standard and space-time separated kMeans++; $m = 500$), and VIF ($m_v = 30$, $m = 500$) approximations.

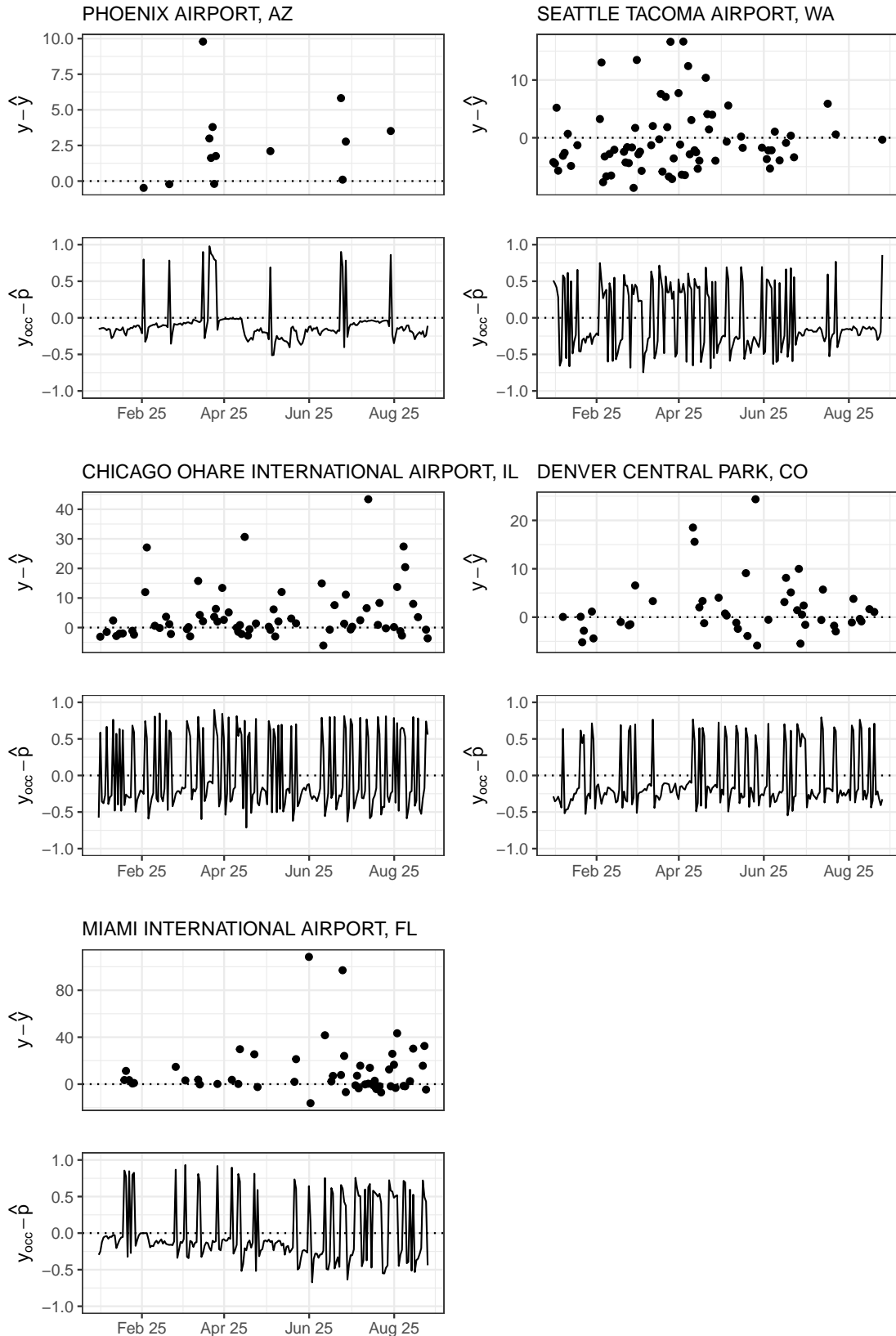


Figure 24: One-day-ahead precipitation forecast residuals (conditional on rain) and rain-occurrence errors for five representative GHCN stations across the full prediction period.

Date	σ	λ	σ_1^2	a	c	α	β	δ	Time range	Space range
Dec 24	3.111	1.415	16.212	0.232	9.92e-07	0.905	0.260	2.489	3.3 days	3,263 km
Jan 25	3.105	1.422	15.450	0.232	9.95e-07	0.889	0.261	2.484	3.3 days	3,338 km
Feb 25	3.101	1.418	16.234	0.231	9.98e-07	0.885	0.262	2.436	3.4 days	3,419 km
Mar 25	3.118	1.421	12.471	0.231	1.01e-06	0.879	0.267	2.408	3.5 days	2,966 km
Apr 25	3.229	1.429	16.465	0.230	1.07e-06	0.872	0.263	2.385	3.6 days	2,800 km
May 25	3.234	1.453	18.197	0.230	1.07e-06	0.867	0.264	2.381	3.6 days	2,800 km
Jun 25	3.276	1.464	18.863	0.230	1.07e-06	0.863	0.266	2.361	3.6 days	2,800 km
Jul 25	3.415	1.508	18.286	0.230	1.08e-06	0.860	0.265	2.353	3.7 days	2,774 km

Table 10: Estimated auxiliary and covariance parameters for the VIF model at each re-estimation, with effective ranges reported as the time or distance at which correlation decays to 0.05.

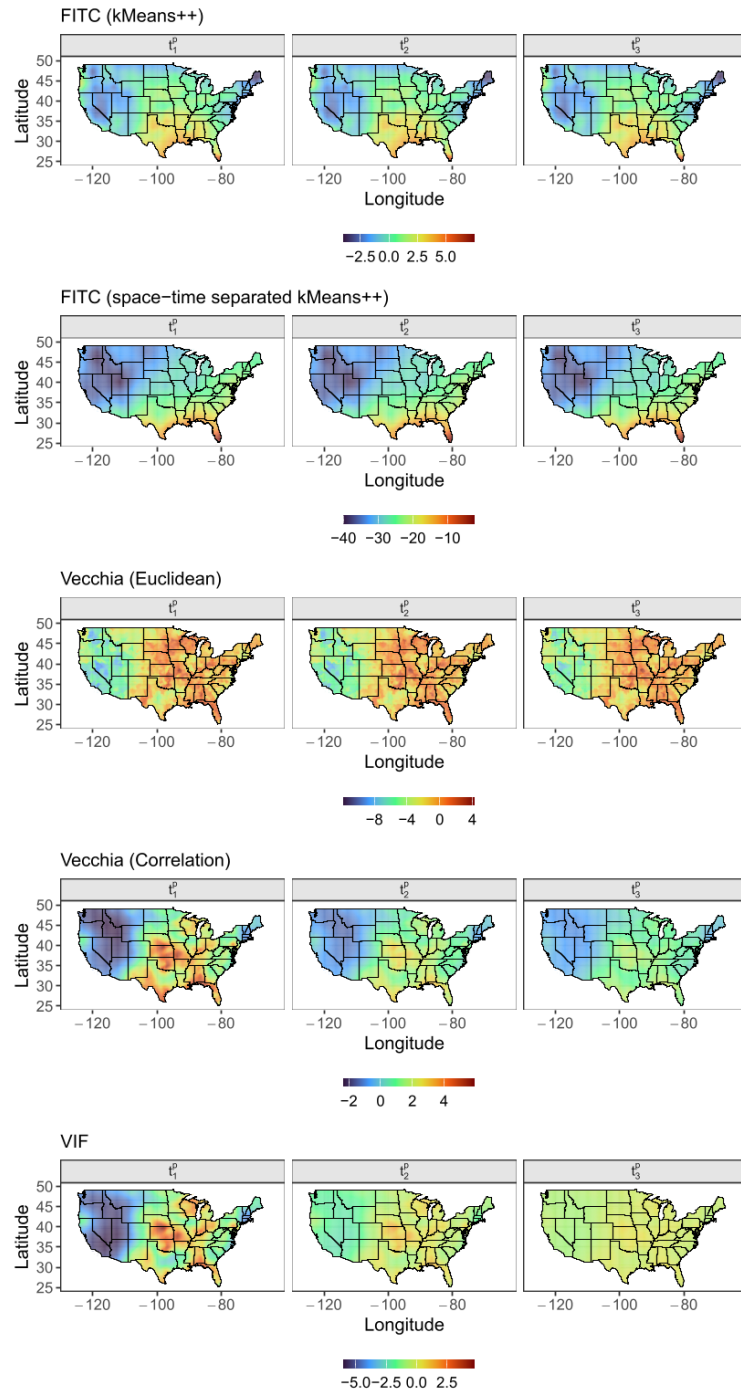


Figure 25: Estimated GP random effects at the final re-estimation step for the precipitation data across the conterminous United States for multiple temporal lags, shown for the Vecchia (Euclidean and correlation-based), FITC (standard and space-time separated kMeans++), and VIF approximations.

F.2 Randomized PIT reliability diagrams (precipitation)

The randomized PIT reliability diagrams for precipitation in Figure 26 evaluate calibration of the full zero-censored power-transformed normal (ZC-PTN) predictive distribution, jointly assessing precipitation occurrence and positive amounts.

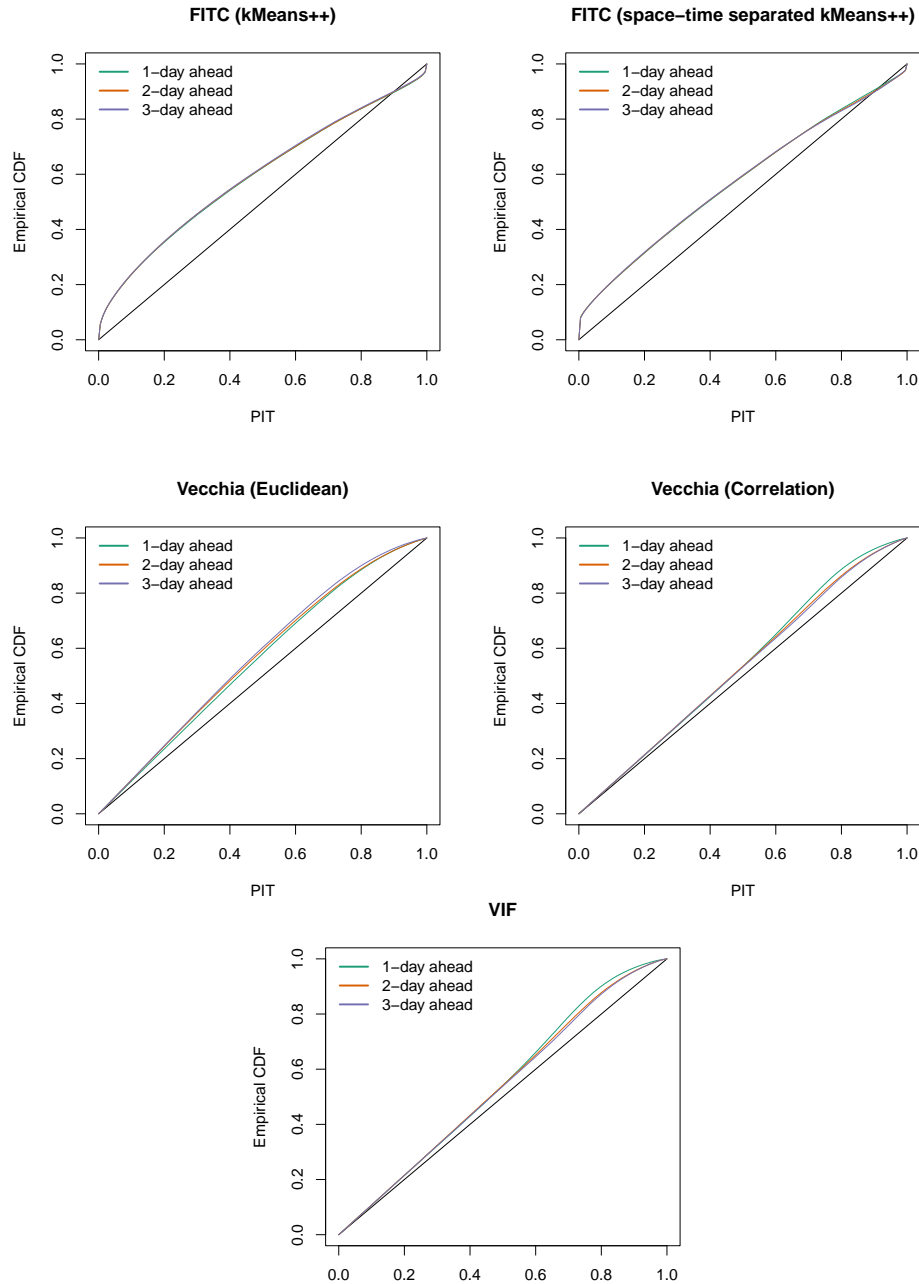


Figure 26: Randomized PIT reliability diagrams for precipitation forecasts using VIF, FITC, and Vecchia approximations under the ZC-PTN likelihood. Curves show uniform(0,1) QQ-plots for the empirical PIT CDFs for forecast instances pooled over all stations and shown separately for each lead time from one to three days. The black diagonal represents perfect calibration.

Appendix References

S. Abdullah, F. Alamri, P. Nag, Y. Sun, H. Ltaief, D. E. Keyes, and M. G. Genton. The second competition on spatial statistics for large datasets. *arXiv preprint arXiv:2211.03119*, 2022.

M. Bevilacqua, V. Morales-Oñate, and C. Caamaño-Carrillo. GeoModels: Procedures for Gaussian and non Gaussian geostatistical (large) data analysis. *R package version*, 1(2):666, 2022.

W. Chen, Y. Li, B. J. Reich, and Y. Sun. Deepkriging: Spatially dependent deep neural networks for spatial prediction. *arXiv preprint arXiv:2007.11972*, 2020.